A cytomegalovirus immunevasin triggers integrated stress response-dependent reorganization of the endoplasmic reticulum.

Running Title: HCMV UL148 reorganizes the ER.

Hongbo Zhang[a,1], Clarissa Read[d,e,1], Christopher C. Nguyen[a,1], Mohammed N.A. Siddiquey[a], Chaowei Shang[c], Cameron M. Hall[a], Jens von Einem[d], and Jeremy P. Kamil[a,b #]

[a]Department of Microbiology and Immunology,

[b]Center for Molecular and Tumor Virology

[c]Research Core Facility

LSU Health Sciences Center, Shreveport, Louisiana, USA

[d] Institute of Virology, Ulm University Medical Center,

[e]Central Facility for Electron Microscopy, Ulm University

Ulm, Germany

[1] these authors contributed equally to the study

Running Head: HCMV UL148 Remodels the ER

[#]Address correspondence to Jeremy P. Kamil, jkamil@lsuhsc.edu

ABSTRACT. Human cytomegalovirus (HCMV) encodes an ER-resident glycoprotein, UL148, which activates the unfolded protein response (UPR) but is fully dispensable for viral replication in cultured cells. Hence, its previously ascribed roles in immune evasion and modulation of viral cell tropism are hypothesized to cause ER stress. Here, we show that UL148 is necessary and sufficient to drive the formation of large ER-derived structures that occupy up to 7% of the infected cell cytosol. The structures are found to be sites where UL148 coalesces together with cellular proteins involved in ER quality control, such as Hrd1 and EDEM1. Ultrastructural analyses of the structures reveal tortuous, densely packed segments of collapsed ER which connect to distended cisternae. Notably, UL148 accumulates in a detergent-insoluble form during infection while a homologous rhesus cytomegalovirus immunevasin that fails to cause ER reorganization remains soluble. During induced ectopic expression of a UL148-GFP fusion protein, punctate signals traffic to accumulate at prominent structures that exhibit poor recovery of fluorescence after photobleaching. Small molecule blockade of the integrated stress response (ISR) prevents the formation of puncta, leading to a uniform reticular fluorescent signal. Accordingly, ISR inhibition during HCMV infection abolishes the coalescence of UL148 and Hrd1 into discrete structures. Given that UL148 stabilizes immature forms of a receptor binding subunit for a viral envelope glycoprotein complex of pivotal importance for HCMV infectivity, which is otherwise particularly susceptible to ER associated degradation, our results imply that stress-dependent ER remodeling contributes to viral cell tropism.

48 **IMPORTANCE.**

49 Perturbations to ER morphology occur during infection with various intracellular
50 pathogens and in certain genetic disorders. We identify that an HCMV gene product,
51 UL148, profoundly reorganizes the ER during infection, and is sufficient to do so when
52 expressed on its own. Our results reveal that UL148-dependent reorganization of the
53 ER is a prominent feature of HCMV infected cells. Moreover, we find that this example
54 of virally induced organelle remodeling requires the integrated stress response (ISR), a
55 stress adaptation pathway that contributes to a number of disease states. Since ER
56 reorganization accompanies the roles of UL148 in HCMV cell tropism and intracellular
57 retention of the immune cell co-stimulatory ligand CD58, our results may have
58 implications for understanding the mechanisms involved. Furthermore, our findings
59 provide a basis to utilize UL148 as a tool to investigate organelle responses to stress
60 and to identify novel drugs targeting the ISR.

INTRODUCTION.

UL148 is a human cytomegalovirus (HCMV) ER-resident glycoprotein that plays roles in evasion of cell-mediated immunity and shows intriguing effects on cell tropism. During infection of epithelial cells, viruses disrupted for *UL148* replicate to produce roughly 100-fold enhanced levels of infectious progeny virions compared to wildtype (1). These effects correlate with reduced expression of glycoprotein O (gO), a subunit of a heterotrimeric viral glycoprotein H (gH) / glycoprotein L (gL) complex (gH/gL/gO) on the virion envelope that is required for the infectivity of cell-free virions (2-4), and which endows the virus with the capacity to utilize the platelet derived growth factor receptor α (PDGFRα) as an entry receptor (5-7). Accordingly, UL148 has been found to stabilize immature forms of gO prior their assembly into gH/gL/gO heterotrimers (1, 8). Despite that UL148 does not stably associate with gO, the data suggest that it may interact with gH (1).

UL148 also physically associates with CD58 (LFA-3), a co-stimulatory ligand for natural killer cells and T-lymphocytes, preventing its presentation at cell surface (9). Although the mechanisms by which UL148 stabilizes gO and retains CD58 within the ER remain unknown, UL148 strongly contributes to activation of the unfolded protein response (UPR) during infection, and is sufficient to activate the UPR when ectopically expressed in non-infected cells (10). UL148 co-purifies from infected cells with SEL1L, an adaptor subunit of ER-based E3 ubiquitin ligase Hrd1 that plays important roles in ER-associated degradation (ERAD) of terminally misfolded glycoproteins (8). This suggests a physical interaction with ERAD machinery, which may be germane to the mechanism by which UL148 activates the UPR.

84 Here, we show that expression of UL148 is necessary and sufficient to induce
85 unusual ER structures at which large quantities of ER factors involved in glycoprotein
86 quality control accumulate. In electron microscopy analyses, we find that the UL148
87 induced ER-structures are comprised of densely packed, tortuous ER membranes that
88 form connections with tubules of highly distended cisternal space. Our results may
89 have implications for understanding the mechanisms by which UL148 regulates viral cell
90 tropism and contributes to viral evasion of cell-mediated immunity. Further, our findings
91 suggest that ER remodeling events triggered by UL148 are indicative of an adaptive
92 response of eukaryotic cells to proteotoxic stress involving the secretory pathway.
93

RESULTS.

UL148 causes reorganization of ER quality control proteins into unusual globular structures.

The HCMV ER-resident glycoprotein UL148 was previously observed to co-localize with the ER marker calnexin during infection (1). Nonetheless, calnexin staining did not show the uniform reticular pattern characteristic for the ER marker. We later noticed that cells infected with a *UL148*-null virus showed uniform calnexin staining (see below). To formally determine whether UL148 influences calnexin localization, we compared fibroblasts at four days post-infection with either wildtype (TB_WT) or *UL148*-null mutant (TB_148_{STOP}) viruses derived from an infectious bacterial artificial chromosome (BAC) clone of HCMV strain TB40/E (**FIG 1**). In cells infected with wildtype virus, calnexin antibodies stained unusual globular structures at the cell periphery, as expected (1) (**FIG 1A, 1C, SI FIG S1A**). However, in cells infected with the *UL148*-null virus, calnexin staining was uniform throughout the cytosol (**FIG 1B-C**), as would be expected for an ER marker in uninfected cells. The staining pattern for Hrd1, another ER marker, likewise indicated accumulation at unusual globular structures during wildtype HCMV infection, but not during infection with *UL148*-null mutant viruses (**FIG 1, SI FIG S1A**). Because calnexin and Hrd1 staining showed uniform distribution in *UL148*-null virus infected cells, and because *UL148* is fully dispensable for efficient viral replication in fibroblasts (1), these results suggest that redistribution of these ER markers depends on UL148.

As expected (11, 12), antibodies specific for the HCMV envelope glycoprotein, glycoprotein H (gH), stained a juxtanuclear compartment, termed the cytoplasmic virion assembly compartment (cVAC), which does not involve the ER (**FIG 1**). Similarly contrasting staining patterns for Hrd1 and/or calnexin were observed in cells infected with wildtype versus *UL148*-null mutants of clinical HCMV strains Merlin and TR (**FIG S1**). Reciprocally, we restored a functional *UL148* at its native locus in the context of a BAC clone of HCMV strain AD169, which spontaneously lost most of the gene in the course of extensive genetic rearrangements and deletions that accumulated during serial passage in tissue culture. In cells infected with AD169 repaired for UL148, but not the *UL148*-null parental virus, the Hrd1 staining pattern showed obvious aggregation into globular structures (FIG S1).

As similar differences in Hrd1 staining are observed between wildtype and *UL148*-null infections of THP-1 macrophages, ARPE-19 epithelial cells and fibroblasts (**FIG 1, FIG S1**), UL148-dependent reorganization of ER markers occurs in multiple cell types. The calnexin staining pattern seen with four different primary clinical isolates from patient throat swabs likewise indicated punctate globular structures. These observations, taken together with the results from formal comparisons of wildtype versus *UL148*-null mutants of four different BAC-cloned HCMV strains (**FIG 1, FIG S1**), argue that UL148 profoundly affects the ER during natural infection.

We measured the three-dimensional volume of UL148-dependent Hrd1 structures from sixteen cells fixed at 96 hpi with strain TB40/E. On average, the structures occupied 303.3 μm^3 (SEM: +/- 24.8) out of a total cell volume of 7657 μm^3 (SEM:+/- 651.0), as measured using a phalloidin-fluorophore conjugate to detect the

actin cytoskeleton (**FIG 1D-E**). Subtracting the volume of nuclei, as indicated by 4′,6-diamidino-2-phenylindole [DAPI] (average nucleus: 1360 μm^3, SEM:+/-129.4), we calculate that, on average, the structures occupy 5.2% of the cytosolic volume (SEM: +/- 0.61%, range: 2.0% – 7.0%). Based on these findings, taken together with results comparing additional WT versus *UL148*-null mutant HCMV strains (**FIG S1**), we conclude that the UL148-dependent ER structures are a prominent feature of HCMV-infected cells.

UL148 substantially contributes to activation of the unfolded protein response (UPR) during HCMV infection (10), and co-purifies from infected cells with SEL1L (8), an adaptor subunit for the E3 ubiquitin ligase Hrd1, which plays crucial roles in ER-associated degradation (ERAD) of terminally misfolded glycoprotein substrates (13). Hence, the accumulation of Hrd1 and calnexin at unusual structures during wildtype but not *UL148*-null infection may suggest that structures form in response to defects in ER quality control (ERQC) caused by UL148. Under conditions of proteasome inhibition, overexpression of certain misfolded glycoproteins causes cellular factors involved in ERQC, such as calnexin, to compartmentalize from the rest of the ER, while other ER markers such as BiP (Grp78) or protein disulfide isomerase (PDI) remain largely unaltered (14-16).

To gain further insights into the nature of these peculiar ER structures, we set out to develop a more comprehensive understanding of their protein composition by comparing the localization of selected ER markers in cells fixed at 96 h post-infection (hpi) either with TB_148^{HA} (1), a derivative of HCMV strain TB40/E that expresses at the C-terminus of UL148 the nonapeptide epitope YPYDVPDYA from influenza A

hemagglutinin (HA), or with TB_159^{HA}, an isogenic control virus in which we replaced the *UL148* coding sequence with the UL148 homolog from rhesus cytomegalovirus, Rh159, likewise fused at its C-terminus to an HA-tag. We considered the TB_159^{HA} virus to be an appropriate control for the following reasons. Firstly, Rh159 and UL148 exhibit ~30% identity at the amino acid level and both glycoproteins localize to the ER and block cell surface presentation immune cell activating ligands; UL148 retains CD58, a ligand for CD2, while Rh159 retains NKG2D ligands of the MIC- and ULBP families (1, 9, 17). Secondly, Rh159 is expressed from TB_159^{HA} at comparable levels and with similar kinetics observed for UL148 from TB_148^{HA}, and the two viruses replicate indistinguishably in fibroblasts (**FIG 2**). Moreover, Rh159 does not appear to activate the UPR (10), and ERQC markers fail to coalesce into unusual structures during infection with TB_159^{HA} (**FIG 3**). Notably, ER structures likewise fail to occur in rhesus fibroblasts during infection with a recombinant rhesus cytomegalovirus (RhCMV) engineered to express an HA-tag fused at the C-terminus of Rh159 (**FIG S1**). This argues against the possibility that Rh159 requires the context of rhesus cells to redistribute ER markers in a manner analogous to what is seen for UL148 during HCMV infection, and instead suggests that UL148 and Rh159 authentically differ in their effects on the secretory pathway.

In cells infected with TB_148^{HA}, HA antibody staining indicated localization of UL148 to globular structures, as expected (1). Antibody signals during indirect confocal immunofluorescence detection of cellular ER resident proteins involved in ERQC, including calnexin, Hrd1, SEL1L, Herp, valosin containing protein (VCP, p97), and EDEM1, co-localized to a strong degree with signals from HA-tagged UL148 (**FIG 3-4**).

These results indicate that a number of ERQC factors coalesce with UL148 to form prominent globular structures in infected cells. In contrast, uniform ER staining patterns were observed with antibodies specific for PDI and calreticulin (CALR), indicating that these ER markers do not localize to the UL148 structures (**FIGS 3Q, 3S**). Intriguingly, antibody signals detecting reticulon 3 and ribophorin 1, which are markers for smooth ER and rough ER, respectively, each appreciably co-localized with UL148 (HA) signal at the induced structures (**FIGS 3K, 3M)**, which indicates that the structures may involve both rough and smooth ER. LC3B failed to co-localize with the structures (**FIG S2**), as would be expected given that the virus inhibits macroautophagy at late times during infection (18, 19). Nevertheless, we obtained evidence suggesting the induced structures are enriched for a related mammalian ATG8 ortholog, GABARAP (**FIG 3O**).

In cells infected with TB_159^{HA}, all of the ER markers we examined showed uniform, reticular staining, as did the anti-HA signal detecting Rh159 (**FIG 3B, D, F, H, J, L, N, P, R, T**). EDEM1, in addition to showing reticular staining, also labeled puncta associated with the nucleus (**FIG 3J**), which may represent enriched levels of the protein at the rough ER membranes associated with the nuclear envelope, although we cannot exclude the possibility of spurious intranuclear staining. Nonetheless, the punctate nuclear signal for EDEM1 was much less pronounced in the TB_148^{HA} infected cells (**FIG 3I**). GABARAP antibodies stained the cVAC in TB_159^{HA} infected cells, but also showed a much weaker reticular signal that may indicate ER staining. Even though we took steps to block viral Fc receptors, which can cause rabbit antibodies to non-specifically label the cVAC (20), it is plausible that GABARAP antibody signal from the cVAC reflects incomplete blocking of viral Fc receptors. For

both viruses, antibodies specific for syntaxin-6 (STX6) and gH, as expected, stained the juxtanuclear cVAC structure (11, 12, 21), which was previously found to be altogether distinct from the UL148 staining pattern (1) (**FIG S2**).

To quantify the degree of co-localization with UL148, we calculated Pearson's correlation coefficients from a minimum of thirty TB_148^{HA} infected cells per staining condition, comparing the signal overlap for each ER marker to the HA signal from UL148. The correlation coefficients (*r*) for EDEM1, Hrd1, reticulon-3 (RTN3), SEL1L and calnexin ranged from 0.8 to 0.72, which suggests that these proteins extensively co-localize with UL148 at 4 days post-infection (dpi) (**FIG 4**). Meanwhile, GABARAP, VCP, ribophorin-1 (RPN1), and Herp showed *r* values in the range of 0.54 to 0.51, indicating a moderate degree of co-localization with UL148. However, the ER markers CALR and PDI, and the TGN marker syntaxin-6, gave *r* values of close to zero, which confirms that these markers either do not co-localize with UL148 or show only a negligible degree of association with UL148 at the induced structures.

From these results, we conclude that the UL148-dependent ER structures are enriched for cellular markers associated with glycoprotein quality control. In this regard, the structures resemble the "ER quality control (ERQC) compartments" described by G. Lederkremer and colleagues (14, 15, 22). We further conclude that Rh159 cannot substitute for UL148 to redistribute ERQC markers.

VCP and Hrd1 are recruited to incipient UL148 ER structures prior to calnexin.

To determine whether there might be differences in the kinetics of recruitment of ERQC markers during formation of the ER structures, we examined a series of time

231 points from one to four days post-infection (dpi) with wild-type HCMV carrying HA-
232 tagged UL148, staining for three different ERQC markers, calnexin, Hrd1, and VCP,
233 alongside UL148 (HA). At 1 dpi the signal from UL148 was only faintly detected, as
234 expected (1), while each of the ER markers was readily detected, providing a readout of
235 their staining patterns prior to being substantially perturbed by UL148 (**FIG 5**). At 2 dpi,
236 we detected robust anti-HA signal, indicating the presence of UL148. At this time point,
237 UL148 exhibited intense signal at small globular puncta, which we interpret to represent
238 incipient UL148 structures, as well as more diffuse staining of a reticular structure
239 consistent with ER. Calnexin did not appreciably co-localize with the UL148 puncta until
240 at least 3 dpi, and the structures were not readily visualized by calnexin staining until 4
241 dpi (**FIG 5A**). In contrast, signals from Hrd1 and VCP staining were sufficient to mark
242 the UL148 puncta by 2 dpi, which suggests that these markers co-localize with UL148
243 at earlier points during the genesis of the ER structures. Notably, the appearance of
244 Hrd1 at the structures prior to calnexin is consistent with our previous results showing
245 that UL148 co-purifies from infected cells with SEL1L, an adaptor subunit for Hrd1 (8).
246 These results imply that basal elements of the ERAD machinery, exemplified by Hrd1
247 and VCP, may be recruited to UL148-induced ER structures prior to calnexin.
248
249 **Visualization of UL148-induced ER structures by electron microscopy.**
250 To discern the ultrastructural appearance of the UL148 structures and to formally
251 ascertain their relationship to the ER, we carried out transmission electron microscopy
252 (TEM) imaging of wildtype (TB_WT) and *UL148*-null (TB_148$_{STOP}$) infected fibroblasts at
253 5 dpi. In high pressure frozen and freeze-substituted infected fibroblasts, cells with a

high density of viral nucleocapsids within the nucleus were selected for analysis, as this feature indicates late time points during infection when UL148 is abundantly expressed. The TEM results revealed prominent globular and oblong structures in the cytoplasm of wildtype virus infected fibroblasts, but not *UL148*-null infected controls (**FIGS 6-7**). The structures stand out for their high electron-density, which may reflect the abundance of ERQC proteins together with UL148 in these structures. Under higher magnification, these areas are characterized by accumulations of densely packed ruffled membranes and membranous material, which appear to be collapsed ER. Further, these membrane accumulations were associated with smooth and partially rough ER structures with seemingly enlarged cisternal space. Further, tomographic reconstruction of scanning transmission electron microscopy (STEM) data suggest that densely packed ER cisternae within the structures are interconnected and continuous in three-dimensional space (**FIG 8B-C, SI Movie S1**).

UL148 accumulates in a detergent-insoluble form during infection.

Disease-associated variants of certain cellular proteins, such as the A103E mutant of the calcium channel Orai1, and the E342K “Z” variant of alpha-1 antitrypsin (Z A1AT), localize to anomalous ER structures reminiscent of those we observe to depend on UL148 (16, 23-26). A103E Orai1 and Z A1AT are found to accumulate in detergent-insoluble forms within the ER or within ER membranes, respectively, which indicates aggregation or polymerization of these proteins, and suggests a mechanism for the formation of ER structures by the proteins (16, 23, 26, 27). We therefore set out to determine whether differences in solubility might correlate with the differing potentials

277 UL148 and Rh159 to cause ER reorganization and to activate the UPR (10). To
278 address this question, we infected fibroblasts with TB_148^{HA} or TB_159^{HA} at MOI 1 and
279 at various times post-infection prepared cell lysates in radioimmunoprecipitation assay
280 (RIPA) buffer. After subjecting the lysates to high-speed centrifugation, we examined
281 the relative levels of UL148 and Rh159 in the detergent-soluble supernatant and
282 detergent-insoluble pellet fractions.

283 A substantial portion of UL148 was detected from the detergent-insoluble
284 fractions at all time points tested (**FIG 9**). Furthermore, the percentage of UL148
285 detected within the insoluble fraction increased over time. In contrast, Rh159 was found
286 only in the detergent-soluble fraction. From these results, we conclude that UL148
287 accumulates in a detergent insoluble form during infection, and that Rh159 does not do
288 so. Because the relative mobility of the anti-HA immunoreactive band detected in
289 soluble and insoluble fractions obtained from TB_148^{HA} infected cells showed a relative
290 mobility of ~35 kD, which is indicative of the mature, endoH-sensitive glycoprotein (1),
291 these findings suggest that UL148 may aggregate or polymerize within the ER.
292

293 **UL148 is sufficient to compartmentalize the ER.**

294 Our data thus far demonstrate that UL148 is necessary during infection to cause
295 redistribution of cellular ER markers for glycoprotein quality control processes, such that
296 substantial portion of the ERQC machinery appears to become sequestered away from
297 the rest of the organelle into novel membranous structures. Because a number of viral
298 proteins that remodel the ER during infection are sufficient to alter ER morphology when
299 ectopically expressed [e.g. (28),(29), reviewed in (30)], we wondered whether UL148

expression is sufficient to induce ER structures akin to those seen during HCMV infection. Making use of existing "tet-on" ARPE-19 epithelial cells that inducibly express of either UL148 or Rh159, each carrying a C-terminal HA-tag (31), we induced transgene expression for 48 h and subsequently stained for various cellular markers for the ER, for ERQC as well as for LC3B and GABARAP, which are ATG8 family proteins that mark autophagosome membranes.

In cells expressing UL148 (i148^{HA}), we observed that calnexin, Hrd1, EDEM1, and VCP co-localize with UL148 at prominent globular structures reminiscent of those observed during infection (**FIG 10**). The respective rough and smooth ER markers ribophorin 1 (RPN1) and reticulon 3 (RTN3), as well as the ATG8 proteins LC3B and GABARAP likewise co-localized to the UL148-induced structures. However, PDI and CALR each failed to substantially co-localize with UL148 at the structures (**FIG 10**), or at best showed only limited co-localization, consistent with our results from infected cells (**FIG 3-4**). Signals from antibodies specific for a KDEL motif important for ER retrieval of luminal ER residents, such as BiP, likewise showed only limited co-localization with UL148. These results suggest that large portions of the ER are not involved in the UL148 structures.

In cells expressing the UL148 homolog Rh159 (i159^{HA}), we detected uniform cytoplasmic distribution of ER markers, as well as of HA-tagged Rh159, similar to what we observed during infection with the recombinant HCMV TB_159^{HA} (**FIG 3**). Furthermore, In this setting the staining patterns for the ATG8 family proteins LC3B and GABARAP failed to indicate any notable structures. Consistent with our previous study showing that UL148, but not Rh159, is sufficient to activate the UPR (10), we observed

accumulation of ATF4 and phosphorylated eIF2α during induction of UL148 but not Rh159 (**FIG 11A**). Importantly, the intensity of HA signals detecting UL148 and Rh159 indicated that both ER resident immunevasins accumulate at roughly comparable levels following dox induction. This argues against the possibility that gross differences in induced transgene expression might account for their differing effects on UPR activation and on the staining patterns for ER markers.

Pearson's correlation coefficient values were calculated to quantify the extent of colocalization between UL148 and various cellular markers: EDEM1, Hrd1, VCP, calnexin (CNX), RTN3, SEL1L, LC3B, and PDI (**FIG 11B**). The results quantitatively buttress the immunofluorescent staining data shown in FIG 10. From these results, we conclude that no other HCMV gene products are required for UL148 to cause ERQC factors to segregate into discrete compartments. Hence, UL148 is sufficient to cause large-scale reorganization of ERQC markers. Moreover, these findings suggest that reorganization of ER markers into discrete structures may be related to the propensity of UL148 to induce ER stress.

To determine whether UL148-dependent ER remodeling could be visualized in real-time using live cell imaging, we constructed "tet-on" lentiviral vectors that inducibly express either UL148 or Rh159 fused at their predicted C-terminal cytoplasmic tails to the enhanced green fluorescent protein (GFP) from *Aequorea victoria* (32). Following lentiviral transduction, puromycin-resistant ARPE-19 were isolated and subsequently subjected to fluorescence-activated cell sorting (FACS) to enrich for cells that expressed GFP signal following dox treatment. The resulting cell populations, which

inducibly express either UL148-GFP or Rh159-GFP, were designated i148^{GFP} and i159^{GFP}, respectively.

In live cell imaging studies, we observed that the GFP signal in dox-induced i148^{GFP} cells first appeared in a reticular, largely uniform pattern, which was readily visible at 5 h post-induction. However, by 9 h post-induction punctate signals began to appear. These puncta were observed to traffic to sites of large-scale accumulation, where large fluorescent structures progressively increased in size up until the termination of the experiment at 19 h (**FIG 12A, SI Movie 2**). In contrast, i159^{GFP} cells exhibited a largely diffuse, reticular GFP signal at all time points monitored subsequent to transgene induction (**FIG 12B, SI Movie 3**). Our live cell imaging results thus recapitulated the differences in the HA-staining patterns that we had observed between dox-induced i148^{HA} and i159^{HA} cells following fixation, as well as those between HA signals during HCMV infection with TB_148^{HA} and TB_159^{HA} (**FIGS 1, 3, 10, SI Fig S1**).

UL148-GFP structures exhibit poor recovery of fluorescence after photobleaching.

To determine whether the protein contents of the UL148 induced structures would exhibit decreased mobility compared to non-perturbed ER regions, we carried out fluorescence recovery after photobleaching (FRAP) studies. We photobleached regions of GFP signal in i148^{GFP} or i159^{GFP} ARPE-19 cells that had been induced for transgene expression for 24 h, and then monitored recovery of fluorescence over a 5 min time period. In Rh159-GFP expressing cells (i159^{GFP}), fluorescence nearly recovered to pre-bleach levels within 3 min, and by 5 min fully recovered (**FIG 13D**). In contrast, when

368 we photobleached a prominent UL148-GFP structure, the GFP signal failed to
369 appreciably recover fluorescence during the same 5 min time period (**FIG 13E**).
370 Nonetheless, an area of reticular GFP signal in an i148^{GFP} cell that presumably
371 represents a region of the ER not involved in an anomalous structure, recovered
372 fluorescent signal with kinetics similar to those observed during Rh159-GFP expression.
373 These results suggested to us that UL148 structures do not exchange their contents as
374 efficiently as unperturbed ER, or that at least the UL148-GFP within the structures is not
375 able to be replaced rapidly with UL148-GFP fusion protein from other portions of the
376 organelle.
377
378 **Ectopically-expressed UL148 is degraded by proteasomes and not by autophagy.**
379 The UL148 ER structures were found to be enriched with proteins such as Hrd1,
380 SEL1L, EDEM, and VCP (**FIG 3-4**, **10-11B**), which are posited to play key roles in
381 ERAD, a process during which misfolded glycoproteins are recognized, processed, and
382 dislocated across the ER membrane for degradation at cytosolic proteasomes.
383 However, we also detected elements of the machinery for autophagy in close
384 association with the UL148 structures. Namely, the mammalian ATG8 ortholog
385 GABARAP co-localized with UL148 during infection (**FIG 3-4**), and both GABARAP and
386 another ATG8 ortholog, LC3B, were found to co-localized with UL148 at the ER
387 structures during ectopic expression of UL148 (**FIG 10, 11B**). Therefore, we wished to
388 determine whether UL148 is degraded by the proteasome, as would be consistent with
389 conventional ERAD, or by the lysosome, which would suggest a role for autophagy-

related processes, such as selective autophagy of the ER (33), in dispensing with UL148, and presumably, in resolving the ER perturbations.

As a first step, we conducted a live-cell imaging "washout" experiment in which i148^{GFP} cells were induced for transgene expression for 24 h, after which the growth medium containing the transgene inducing agent (dox) was replaced with medium lacking dox. During a 22 h imaging period following dox-washout, we observed the structures to become progressively smaller as the reticular and punctate GFP signals gradually abated (**FIG 14A, SI Movie S7**). Because the results suggested that UL148-GFP structures could be resolved over time, we induced UL148-GFP in tet-on ARPE-19 cells (i148^{gfp}) for 24 h, washed out the inducing agent (dox), and then applied either epoxomicin (20 μM), an irreversible inhibitor of the proteasome (34), or folimycin (115 nM), a proton pump inhibitor that blocks autophagosome maturation and impedes the lysosome-dependent protein degradation (35, 36). Of the two inhibitors, only epoxomicin markedly stabilized UL148, as evidenced by the sustained Western blot signal for both GFP and UL148 in this condition relative to either DMSO carrier or folimycin treatments (**FIG 14B-C**). Despite that folimycin treatment had no obvious effect on UL148-GFP levels, the drug markedly increased the levels of LC3B-II, as would be expected with the lysosomal proton pump inhibitor. From these results, we conclude that ectopically expressed UL148 is primarily degraded via a proteasome-dependent mechanism.

UL148 requires the integrated stress response to cause ER reorganization.

We previously reported that UL148 triggers the UPR during ectopic expression, and that UL148 contributes to activation of the PKR-like ER kinase (PERK) and inositol requiring enzyme 1 (IRE1) during infection (10). Although we failed to find any effect of small interfering RNA (siRNA) or drug treatments targeting IRE1 on UL148-dependent ER remodeling (not shown), we did observe that siRNA directed at PERK caused UL148 to fail to form puncta or to co-localize with Hrd1 (not shown). Furthermore, the literature suggests that formation of ERQC compartments requires PERK (37). PERK responds to ER stress by activating the integrated stress response (ISR). In particular, PERK phosphorylates eIF2α at Ser51 (eIF2α-P), and the accumulation of eIF2α-P causes global attenuation of mRNA translation whilst paradoxically stimulating translation of select mRNAs, such as those encoding ATF4 and CHOP, which play roles in adaptation to stress (38). Stress-regulated translation of such mRNAs involves small upstream open reading frames (uORFs) in their 5' untranslated regions that ordinarily suppress translation under basal conditions (39, 40).

To examine whether ER remodeling in response to UL148 requires the ISR, we turned to a well characterized small molecule inhibitor of stress-regulated translation, ISRIB (41-45). ISRIB is thought to act as a "molecular staple" that holds the guanine nucleotide exchange factor eIF2B in an active decameric configuration (43-46), such that eIF2B will continue to generate ternary complex (eIF2•GTP•Met-tRNAi) necessary for new cycles of translational initiation, despite the presence of phospho-eIF2α (Ser51). Because PERK is the kinase that phosphorylates eIF2α in response to ER stress (47, 48), we also tested for effects of the PERK inhibitor GSK2606414 (49). Having confirmed that ISRIB and GSK260641 do not negatively impact UL148 expression

during dox-induction of UL148-GFP **(FIG 15A-B)**, we treated i148^{GFP} cells with 200 nM ISRIB, 1.1 μM GSK260641, or DMSO vehicle control, and carried out live cell imaging during contemporaneous dox induction of UL148-GFP fusion protein.

Strikingly, ISRIB and GSK6060414 virtually abolished the formation of UL148 puncta through 13 h post induction (dox addition), a time point at which the DMSO control condition showed abundant large structures (**FIG 15C-E, SI Movies 8-10**). Based on our previous findings (**FIGs 1-3, 6-7, 10)**, we interpret the formation and subsequent large-scale aggregation of UL148-GFP puncta to faithfully indicate of ER reorganization in response to UL148. Therefore, these results suggested to us that pharmacological treatments that inhibit the ISR and PERK prevent UL148 induced remodeling of the ER, which further implies that ER remodeling in response to ER stress requires stress-regulated translation.

Since our results with ISRIB and GSK6060414 suggest that the ISR is required for UL148 mediated ER remodeling during ectopic expression of UL148, we next asked whether these pharmacological agents would prevent UL148-dependent ER remodeling in the physiologically authentic context of HCMV infection. However, our live cell imaging studies with ISRIB and GSK6060414 indicated that following a pronounced delay, UL148-GFP puncta nonetheless began to appear by ~19 h post treatment (**FIG 15D-E, SI Movies 9-10**), which suggested that the pharmacological activity of the drugs might diminish over time. Therefore, in order to ensure that blockade of PERK and the ISR would be sustained over a four-day period that it takes for structures to fully form during HCMV infection, we replenished the drugs every 24 h by replacing the spent

457 media with media containing freshly reconstituted ISRIB, GSK6060414, or DMSO
458 vehicle control.

459 At 4 days postinfection, ER structures were virtually ablated in the ISRIB and
460 GSK2606414 treatment conditions (**FIG 16A**). To quantify these effects, we obtained Z-
461 stacks from a minimum of 30 cells per treatment condition and used Imaris 3D image
462 analysis software to calculate the percentage of Hrd1 signal that coalesced into discrete
463 structures during infection. The results indicated highly significant differences between
464 the DMSO carrier alone setting compared to treatments with either GSK2606414 or
465 ISRIB (**FIG 16B**). In the DMSO control condition, on average, 10% of the Hrd1 signal
466 was found to be associated with the UL148 structures (arithmetic mean; range 5.8% –
467 17.6%), as indicated by structures delimited by HA signal. In the presence of ISRIB or
468 GSK2606414, however, these values were reduced to 2.8% (range: 0.69% – 7.1%) and
469 3.6% (range: 0.8%-6.5%), respectively. Reassuringly, roughly equivalent levels of
470 UL148 were detected in Western blot analyses of protein extracts from drug treated and
471 DMSO control conditions. Therefore, differences in UL148 expression are unlikely to
472 explain the observed failure of UL148 and Hrd1 to coalesce into structures during
473 inhibition of either the ISR or PERK. Meanwhile, ISRIB and GSK2606414 treatments
474 both led to reduced levels of ATF4 accumulation, while the PERK inhibitor alone was
475 able to reduce the levels phospho-eIF2α (Ser51), as indicated by a phospho-specific
476 antibody. Therefore, each of the drugs caused their expected effects on the PERK /
477 eIF2α / ATF4 axis (**FIG 16C-D**).

478 A modest reduction in the levels of the viral envelope glycoprotein B (gB) was
479 observed during treatments with ISRIB or GSK2606414. This may suggest that the ISR

480 is required for optimal expression of the certain viral envelope glycoproteins. Even
481 viruses lacking *UL148* cause high levels of ATF4 accumulation at late times during
482 infection, which is when viral late gene products, such a gB, are expressed at their
483 highest levels (10). Hence, the activity of PERK, and/or ISR regulated translation may
484 be required for optimal expression of viral envelope glycoproteins. Regardless, the
485 PERK inhibitor and ISRIB each prevented the appearance of discrete UL148 ER
486 structures while failing to substantially affect UL148 expression. Therefore, the effects
487 of the two inhibitors on UL148-dependent ER reorganization were fully consistent with
488 those seen during ectopic expression of the immunevasin. Taken together, our findings
489 argue that the ISR is required for UL148 to cause remodeling of the organelle.

DISCUSSION

The ER structures that we have identified are noteworthy in several regards. Firstly, this example of virally-induced ER remodeling is wholly dependent on a single viral gene product, UL148. Of course, there are other examples of individual viral gene products that are necessary to grossly perturb ER morphology during infection which are also found to be sufficient to induce such perturbations [e.g., (28, 29, 50, 51)]. Nonetheless, the ER structures caused by UL148 are— to the best of our knowledge, a hitherto undescribed ultrastructural characteristic of the HCMV infected cell, which is surprising given their size, scale, and prominence. Indeed, the average volume of the structures at 96 h postinfection amounts to roughly 60% of the size of the nucleus of an uninfected human fibroblast [~500 μm^3, (52)]. Although UL148 expression is accompanied by UPR activation, ER reorganization occurs without killing the host cell, even in the setting of ectopic expression when viral functions that inhibit programmed cell death are absent. Nor does UL148 affect the yield of infectious virus during replication in fibroblasts, since *UL148*-null mutant viruses replicate indistinguishably from wildtype parental virus in this cell type (1, 8). As with all enveloped viruses, HCMV requires the host cell secretory pathway to fold and process enormous quantities of viral envelope glycoproteins that endow progeny virions with the molecular machinery for infectivity. It is intriguing to consider how the infected cell tolerates spatial reorganization of ER membranes and the associated glycoprotein quality control machinery without impacting the production of infectious progeny virions.

Furthermore, certain aspects of ER reorganization invoked by UL148 may be novel to cell biology. In particular, the densely packed collapsed ER in close

association with varicosities that we observe to depend on UL148 during infection appear to differ from the ER structures induced by other ER perturbagens. For instance, a hereditary form of childhood cirrhosis caused by the *Z* allele of the alpha-1-antitrypsin (Z-A1AT) gene (*SERPINA*) is characterized by polymerization of Z-A1AT within the ER (25), leading to its accumulation in membrane-delimited inclusions (25, 26, 53). However, Z-A1AT inclusions are not observed to associate with regions of collapsed ER, nor does Z-A1AT suffice to activate the UPR, even though its expression sensitizes cells to other triggers of ER stress (26, 54).

HCMV encodes at least one other ER-resident immunevasin that activates the UPR, US11 (55). UL148 binds the NK-cell and T-cell costimulatory ligand CD58 to prevent its transport to the cell surface while US11 targets the heavy chain of class I major histocompatibility complex (MHC) for ER-associated degradation (56, 57). UL148 causes CD58 to accumulate as an immature glycoform, presumably within the ER, but does not lead to any obvious decrease in its overall abundance (9). Albeit that intracellular forms of CD58 appear to be refractory to detection by standard indirect immunofluorescence protocols (not shown), it seems reasonable to hypothesize that UL148 sequesters CD58 into the unusual ER structures that it induces. Moreover, our detergent solubility results suggest that UL148 may form aggregates or polymers in the course of preventing CD58 presentation at the cell surface (FIG 9). It is worth noting that UL148, an immunevasin targeting CD58, induces dramatic morphologic rearrangements of the ER, while another HCMV immunevasin, US11, targeting MHC class I for degradation evidently does not do so, even though both trigger ER stress. Nonetheless, it seems unlikely that retention of CD58 would be required for ER

reorganization. In fact, the capacity of UL148 to retain CD58 may be functionally separable from its peculiar effects on the morphology and organization of the ER.

Despite that the relationship between the mechanism for CD58 retention and the formation of UL148-dependent ER structures remains unresolved, our findings may suggest a mechanism to explain the influence of UL148 on the tropism of the virus for epithelial cells. These effects, exemplified by a ~100-fold replication advantage of *UL148*-null viruses during infection of epithelial cells, correlate with decreased expression of glycoprotein O (gO), a viral envelope glycoprotein, both in virions and in infected cells (1). We previously reported that gO behaves as a constitutive ERAD substrate during infection and that immature, newly synthesized forms of gO show enhanced stability in the presence of UL148 (8). We now show that UL148 causes large-scale sequestration of cellular factors important for ERAD, such as the ER mannosidase EDEM1 and the E3 ubiquitin ligase SEL1L/Hrd1, into large membranous structures. Moreover, the reticular ER, as indicated by the staining patterns of antibodies specific for calreticulin, PDI, and the KDEL motif, appears to remain largely intact following UL148-induced ER reorganization (FIGs 3, 10). Since these observations indicate that UL148 depletes ERAD factors from the ER during the formation of the unusual structures, regions of ER not drawn into the structures might be expected to offer a more permissive folding environment for polypeptides, such as gO, which either fold slowly or inefficiently assemble into multiprotein complexes.

Based on these observations, one might hypothesize that UL148 alters ER proteostasis by physically dislocating (or sequestering) key elements of the “mannose removal time clock” system that marks poorly folding glycoproteins for destruction via

559 ERAD (58, 59). Because gO is both the defining subunit of the heterotrimeric gH/gL/gO
560 envelope glycoprotein complex that governs HCMV entry and cell tropism (5-7, 60, 61),
561 and a constitutive ERAD substrate (1, 8), the hypothesis that ER reorganization is
562 required for the effects of UL148 on HCMV cell tropism does not seem unreasonable.
563 Going forward, it will be crucial to determine whether classical ERAD substrates, such
564 as the null Hong Kong variant of alpha-1-antitrypsin (62, 63) or ribophorin-332 (64, 65),
565 are stabilized during UL148 expression, as would be predicted if UL148 shifts ER
566 proteostasis to negatively modulate ERAD.

567 In addition to having found that factors involved in proteasomal ERAD, such as
568 Hrd1 and EDEM1, are enriched at the UL148 structures, we observed that GABARAP,
569 a mammalian ortholog of yeast ATG8, localizes to the UL148 ER structures during
570 infection, and that another ATG8 ortholog, LC3B, and GABARAP both associate with
571 the structures during ectopic expression of UL148. This may suggest roles for
572 autophagy-related pathways in UL148-dependent reorganization of the organelle.
573 Since our results indicate that UL148 is degraded by a proteasome-dependent pathway
574 and not by lysosomes, it seems unlikely that selective autophagy of the ER is directly
575 involved in recycling or degrading these ER structures. Nonetheless, ATG8 family
576 proteins may contribute to formation of large structures, vis-a-vis the trafficking of
577 UL148-GFP puncta observed during our live cell imaging studies (FIGs 12, 15, Movies
578 S2, S8). The literature indicates that misfolded proteins traffic in a microtubule (MT)-
579 dependent manner to form pericentriolar structures termed aggresomes, which in the
580 case of ERAD substrates such as the ΔF508 mutant of the cystic fibrosis
581 transmembrane conductance regulator (CFTR), contain deglycosylated protein that

582 presumably has already undergone dislocation from the ER (66, 67). ATG8 family
583 proteins such as LC3B and GABARAP not only play roles in degradation of substrates
584 via macroautophagy, but also bind MTs and recruit machinery for MT-dependent
585 transport of cargos (68-70). Therefore, GABARAP and LC3B may be important for the
586 recruitment of cellular machinery that transports perturbed ER cargoes to sites of large-
587 scale accumulation.

588 Although our results argue that the ISR is required for ER reorganization during
589 UL148 expression, precisely how UL148 triggers ER stress remains unknown. UL148
590 has been found to co-purify from cells with SEL1L, a component of the ERAD
591 machinery. Thus, it seems plausible that UL148 may inhibit the Hrd1/SEL1L complex,
592 which would cause the buildup of unfolded proteins and thus trigger the UPR. However,
593 inhibition of ERAD in and of itself seems unlikely to account for the formation of ER
594 structures. Another non-mutually exclusive possibility is that UL148 multimerizes or
595 aggregates in a manner that constricts the ER lumen. For instance, the assembly of
596 UL148 molecules on opposite sides of the ER lumen might constrict the organelle in a
597 manner consistent with the collapsed regions of ER observed in our EM results (FIGs 6,
598 8).

599 Additional work will certainly be needed to decipher the molecular mechanisms
600 by which UL148 causes reorganization of the ER, and to determine its physiological
601 relevance to viral biology. Nonetheless, we have shown that UL148, when fused to a
602 fluorescent protein (FP), suffices both to trigger and to indicate the presence of a
603 functional ISR (FIGs 15-16). Hence, UL148-FP fusions may prove useful in high
604 throughput chemical-genetic screens to identify novel small molecule inhibitors of the

ISR as well as to identify cellular genes involved in stress-dependent remodeling of the ER. Interestingly, the two pharmacological agents that block UL148-dependent ER remodeling, ISRIB and GSK2606414, are known to prevent the formation of stress granules (SGs) (42, 71). SGs are comprised of condensed aggregates of protein and RNA which occur due to stalled mRNA translation in the context of disease states, such as amyotrophic lateral sclerosis (72), as well as during treatments with toxic agents such as arsenite (42, 71). It is fascinating to consider that mechanistic parallels exist between the formation of SGs and the UL148-dependent reorganization of the ER. Moreover, given the broad importance macromolecular aggregation in pathological conditions such as neurodegenerative diseases (73), certain of which also involve defects in ER proteostasis and aberrant activation of the UPR, UL148 may hold promise as tool to discover new agents to ameliorate disease.

MATERIALS AND METHODS.

Cells and virus.

hTERT-immortalized human foreskin fibroblasts (8), derived from ATCC HFF-1 cells (SCRC-1041) were maintained in Dulbecco's modified Eagle's medium supplemented with 5%-10% newborn calf serum (Millipore Sigma) and antibiotics (complete DMEM) exactly as described previously (8). i148^{HA} and i159^{HA} ARPE-19 epithelial cells (10), which upon treatment with 100 ng/mL doxycycline, express HA-tagged UL148 or Rh159, respectively, were likewise maintained in complete DMEM. For live cell imaging studies, i148^{HA} and i159^{HA} ARPE-19 were maintained in Opti-MEM (Thermo Fisher) supplemented with 3% certified tet-approved fetal bovine serum (FBS), 20 µg/mL gentamicin sulfate, 1 µg/mL puromycin HCl and 10 µg/mL ciprofloxacin HCl. Telomerase-immortalized rhesus fibroblasts (74) were a kind gift of Peter A. Barry, and were maintained in complete DMEM. The acute monocytic leukemia cell line THP-1 (TIB-202) was obtained from ATCC (Manassas, VA) and maintained as suspension cultures in RPMI 1640 medium supplemented with 10% FBS (Millipore Sigma) and antibiotics (10 µg/mL ciprofloxacin and 25 µg/mL gentamicin). THP-1 were differentiated into adherent macrophages by incubating for 48 h in the presence of 100 nM 2-O-tetradecanoylphorbol 13-acetate (Millipore Sigma), and subsequently infected with the indicated viruses at an MOI of 5 $TCID_{50}$/cell.

Infectious bacterial artificial chromosome (BAC) clones of the following HCMV strains were used for this study: TB40/E (also known as TB40-BAC4 or TB_WT) (75) as well as its derivatives TB_148^{HA} and TB_148$_{STOP}$, which were used in our previous

641 studies (1, 8, 10); TR (TR*gfp*) (76, 77); Merlin repaired for *UL128* and *RL13* harboring
642 *tetO* sequences upstream of *UL131* (pAL1393) (78); AD169 repaired for *UL131*
643 (AD_r131)(1, 79) and AD_r131_148^{HA}, a derivative of AD_r131 that carries a full length
644 UL148 (from strain TB40/E) tagged with an HA-epitope at the original *UL148* locus (8).
645 An infectious BAC clone of rhesus CMV (RhCMV) strain 68-1 (80) and a derivative that
646 expresses an HA-tagged Rh159 (details below) were also used for certain experiments.
647 The methods used for reconstitution of HCMV from purified BAC DNA, cultivation of
648 virus and preparation of stocks, including ultracentrifugation through sorbitol cushions
649 and determination of infectious titers by tissue culture infectious dose 50 ($TCID_{50}$) assay
650 have been described elsewhere (8, 10).
651
652 **Construction of recombinant viruses and new plasmids for the study.**
653 New recombinant viruses for this study were derived from BAC-cloned HCMV
654 and RhCMVs using *en passant* mutagenesis in GS1783 *E. coli,* a strain K12 derivative
655 that expresses the homing endonuclease I-SceI upon treatment with L-(+)-arabinose
656 (81, 82). Recombinant BACs were confirmed by Sanger DNA sequencing of the
657 modified regions, which was performed by Genewiz, Inc. (Piscataway, NJ) (not shown).
658 Oligonucleotide primers for construction of recombinant viruses and plasmids were
659 custom synthesized by Integrated DNA Technologies (Coralville, IA); sequences are
660 provided in **Table S1**. Type II restriction endonucleases, T4 DNA ligase, and Gibson
661 assembly reagents (NEB HiFi Assembly Master Mix) for generation of recombinant
662 DNAs and for routine molecular cloning and subcloning procedures were obtained from

New England Biolabs (Ipswitch, MA). KOD Hot Start DNA polymerase (EMD Millipore) was used for all PCR reactions.

To construct TB_159^{HA}, a strain TB40/E derivative in which the UL148 open reading frame is replaced by Rh159 we carried out the following steps. Primers Rh159_Fw and Rh159_HA_Rv were used to amplify and HA-tag the *Rh159* ORF from pcDNA3.1+_Rh159_IRES_GFP (a gift from Klaus Früh, OHSU). The PCR product was inserted into EcoRV-digested pEF1α using Gibson assembly. A PCR product containing an ISce-I excisable kanamycin cassette was amplified from TB_148^{HA}_*ISce-Kan* integrate BAC (1) using primers PpuISceKanGibs_Fw and PpuISceKanGibs _Rv and Gibson-assembled into PpuMI-digested pEF1α_Rh159 plasmid to yield plasmid pEF1α_Rh159_ISceKan. Primers Rh159_Fw_recomb and Rh159_Rv_recomb were used to generate a PCR product from template plasmid pEF1α_Rh159_ISceKan. The PCR product was electroporated into GS1783 E. coli harboring the TB_148^{HA} BAC, and Kan^r colonies harboring TB_Δ148_Rh159_ISceKan integrate BACs were isolated on Luria-Bertiani agar plates. Bacterial colonies representing kanamycin resistant integrates were obtained and were subsequently resolved to 'scarlessly' remove the positive selection marker by standard *en passant* protocols (81, 82) to yield TB_Δ148_Rh159^{HA}, which we abbreviate herein as TB_159^{HA}. TB_159^{HA} was sequence-confirmed using primers TB_Rh159HA_seq_Fw and REV TB_Rh159HA_seq. Similar strategies were used to modify the RhCMV 68-1 BAC (80) to incorporate sequences encoding an HA-epitope immediately before the stop codon of *Rh159*. An *en passant* strategy in which a shuttle plasmid carrying *I-SceI-Kan^r* disrupted by in-frame nonsense codons was used insert premature nonsense codons in

686 the *UL148* CDS in the context of HCMV strains Merlin (pAL1393) and TR (TR*gfp*), and
687 was applied as described previously for generating TB_148$_{STOP}$, the UL148$_{STOP}$ mutant
688 of strain TB40/E (8).
689 To construct "tet-on" lentivirus vector plasmids containing UL148 fused to GFP,
690 we used primers Gibs_eGFP_Rv and 148_eGFP_Fw to amplify the GFP gene from a
691 dsDNA gBlock, EGFP-P2A-3XHA, synthesized by Integrated DNA Technologies
692 (Coralville, IA), which was a gift of Matthew D. Woolard (LSU Health Sciences Center,
693 Shreveport, LA). In a separate PCR, the *UL148* gene was amplified from plasmid
694 pcDNA3.1-UL148^{HA} (10) using primers Gib_148_Fw and 148_noStopRv. The two
695 products were assembled, using Gibson Assembly, together with EcoRV opened
696 pcDNA3.1(+) (Invitrogen) to produce pcDNA3.1-UL148-GFP. After confirming the
697 absence of spurious mutations by Sanger DNA sequencing (Genewiz, not shown), the
698 *UL148-GFP* cassette from pcDNA3.1-UL148-GFP was released by EcoRI and NotI
699 digestion and ligated into pOUPc turboRFP-link plasmid which had been linearized
700 using the same restriction sites. pOUPc turboRFP-link is a derivative of lentiviral vector
701 pOUPc (10) that was constructed by reinsertion of turboRFP (tRFP). Briefly, tRFP was
702 amplified from the original pOUPc-turboRFP using primer pair tRFP linker Fw and tRFP
703 linker Rv and then reinserted by Gibson Assembly with pOUPc turboRFP that had been
704 double-digested using EcoRI and Not I in order to linearize the vector and remove the
705 *turboRFP* (RFP) sequence.
706 To express Rh159 fused to eGFP, primers Gibs_eGFP_Rv and 159_eGFP_Fw
707 were used to amplify the GFP gene from EGFP-P2A-3XHA, and in a separate PCR
708 reaction, primers Gibs_159_Fw and 159_noStop_Rv Rh159 were used to amplify

Rh159 from pcDNA3.1-Rh159^{HA} (10). The latter two PCR products were assembled together with EcoRV linearized pcDNA3.1(+) using Gibson Assembly, resulting in plasmid pcDNA3.1-Rh159. The latter plasmid was used as template in a PCR reaction with primers Gibs_Age_159_Fw and Gibs_Mlu_GFP_Rv. The resulting PCR product was Gibson assembled into the lentiviral vector pOUPc (10) which had been double-digested with Mlu I and Age I.

Drug treatments.

The PERK inhibitor, GSK2606414 (49), doxycycline hyclate, and folimycin were obtained from MilliporeSigma (Burlington, MA). ISRIB (41-45) was obtained from MilliporeSigma or APExBio (Boston, MA) and epoxomicin was procured Selleck Chemicals (Houston, TX). ISRIB was dissolved in DMSO to make a 10,000× stock solution (2 mM) and used at a final working concentration of 200 nM. GSK2606414 was dissolved in DMSO to make a 10,000× stock solution (11 mM) and used at a final working concentration of 1.1 μM. Folimycin was prepared as a 1000× (115.46 μM) stock solution in DMSO and used at 115 nM final. Epoxomycin was prepared as a 100× (2 mM) stock solution in DMSO and used at a final concentration of 20 μM.

Confocal microscopy and live-cell imaging. Confocal indirect immunofluorescence microscopy imaging on fixed cells was carried out using Leica TCS SP5 Spectral Confocal Microscope (Leica Microsystems, Heidelberg, Germany) using a Leica HCX PL APO CS 63x/1.4-0.6NA objective under oil immersion, except for the image shown in Figure 1C, which was captured on a Nikon SIM-E and A1R confocal microscopy

732 system (Nikon Instruments, Melville, NY) using a Nikon SR Apo TIRF 100x/1.49NA
733 objective under oil immersion. Images for different fluorophore channels were acquired
734 using sequential scanning. Direct immunofluorescence live cell imaging data were
735 collected using the Nikon SIM-E microscope using a Nikon Apo 60x/1.40NA DIC
736 objective.

737 The 3D projections shown in FIGs 1D and 16A were generated from Z-stacks
738 captured on the Nikon SIM-E / A1R microscope using a Nikon SR Apo TIRF
739 100x/1.49NA objective. For FIG 1D, the 3D projection was generated using NIS-
740 Elements AR Analysis 4.60.00 (64-bit) software (Nikon). For FIG 16A, 3D projections
741 were generated by Imaris x64 9.3.0 software (Bitplane, Inc.) in maximum intensity
742 projection (MIP) mode.

743 For fixed cell imaging experiments other than those shown in Fig S1D, cells were
744 seeded on 12 mm circular, No. 1 thickness microscope cover glass (200121; Azer
745 Scientific, Morgantown, PA). At the indicated times post-treatment and or post-infection,
746 cells were washed with phosphate buffered saline (PBS) [137 mM NaCl, 2.7 mM KCl, 10
747 mM Na_2HPO_4, and 1.8 mM KH_2PO_4, pH 7.4]; fixed for 15 min at room temperature in PBS
748 containing 4% (wt/vol) paraformaldehyde (Fisher Scientific, Waltham, MA), washed in
749 PBS, permeabilized for 10 min using 0.1% Triton X-100 (in PBS), subsequently washed
750 again in PBS, and then blocked for 45 min at 37 °C in PBS containing 5% (vol/vol) normal
751 goat serum (Rockland Immunochemicals, Limerick, PA). Cells were then washed three
752 times in PBS followed by incubation in 1% Human Fc Block (BD Biosciences, San Jose,
753 CA) in PBS, for additional 45 min at 37 °C. Cells were then incubated in the presence of
754 primary antibodies for 1 h at 37 °C or 4 °C overnight, and then washed three times with

PBS containing 0.1% Tween-20 (PBST) for 5 min per wash. Alexa Fluor-labeled goat polyclonal secondary antibodies (all from ThermoFisher Invitrogen, Waltham, MA, see **Table S2**) were used for secondary detection. The slides were then mounted using Prolong Gold anti-fade reagent containing DAPI (ThermoFisher) and placed under a Leica TCS SP5 confocal microscope for image acquisition using a Leica 63× oil immersion objective lens (Leica Microsystems, Buffalo Grove, IL).

For indirect immunofluorescence staining results of primary clinical isolates (SI Fig S1D), four clinical HCMV isolates obtained by routine testing of throat swabs from patients of the Ulm University Medical Center were provided by the diagnostic laboratory of the Institute of Virology in Ulm. Sample material was applied to human fibroblasts and incubated for several days until HCMV-positive cells could be detected. Infected cells were then seeded together with uninfected fibroblasts, incubated for up to 5 days until plaques were formed and processed for indirect immunofluorescence staining. ERQC compartments were detected by staining for calnexin (CNX, E10; Santa Cruz Biotechnology, mouse, 1:50 dilution), the cVAC was detected by staining for HCMV pUL71 (rabbit, 1:500). Secondary antibody used for detection of CNX was Alexa Fluor 555 labeled goat anti-mouse IgG (1:1000) and for pUL71 detection, Alexa Fluor 488 conjugated goat anti-rabbit IgG (1:1000). Confocal images were acquired using the 63× objective of a Zeiss Observer Z1 fluorescence microscope equipped with Apotome and Zen software 2.3 (Carl Zeiss Microscopy GmbH, Jena, Germany).

FRAP. FRAP studies were carried out on using live ARPE-19 cells from the i148^{GFP} and i159^{GFP} populations as follows. Cells were seeded as above for live-cell imaging,

778 induced for transgene expression using dox (100 ng) for 24 h, and then placed on an
779 incubated sample stage of a Nikon A1R SIM-E imaging system equipped with an SR
780 Apo TIRF 100x/1.49NA objective (Nikon). Three rectangular regions in image fields
781 were defined for measurement of (i) background signal, and of two regions with
782 comparable initial GFP signals, (ii) one designated as a control region (no
783 photobleaching) and another for (iii) photobleaching and recovery of signal after
784 photobleaching. Photobleaching of selected regions was carried out for 20 s using 405
785 nm laser light from a LU-N4 laser fiber (Nikon) [power at source: 15 mW, power at
786 objective: 8 mW]. Images and signal intensity measurements were captured every 2 s
787 at a rate of 1 frame per s (488 nm excitation, FITC channel) starting immediately before
788 photobleaching (t=1), and from t=20 s to t=320 s after.
789
790 **Electron microscopy.** Procedures to prepare samples for transmission electron
791 microscopy (TEM) included high-pressure freezing (HPF), freeze substitution, and Epon
792 embedding, which were carried out as described previously (83). Briefly, human
793 fibroblasts were seeded in µ-Slides (Ibidi GmbH, Martinsried, Germany) containing
794 carbon-coated sapphire discs (Engineering Office M. Wohlwend GmbH) 1 day prior to
795 infection at 80 to 90% confluence. Cells were infected with virus overnight at MOI 1.
796 Medium containing viral inocula was replaced with fresh medium the next day. Infected
797 cells on sapphire discs were fixed by using HPF with a Compact 01 high-pressure freezer
798 (Engineering Office M. Wohlwend GmbH, Sennwald, Switzerland) at 5 dpi. Thereafter,
799 cells on sapphire discs were processed by freeze-substitution and subsequently
800 embedded in Epon (Fluka, Buchs, Switzerland). Ultrathin sections of the Epon-embedded

cells were cut with an ultramicrotome (Ultracut UCT; Leica Microsystems, Wetzlar, Germany) and placed on Formvar-coated single-slot grids (Plano GmbH, Wetzlar, Germany). Grids were examined in a Jeol JEM-1400 (Jeol Ltd., Tokyo, Japan) transmission electron microscope equipped with a charge-coupled-device (CCD) camera at an acceleration voltage of 120 kV. Fixation and embedding of infected cells for scanning transmission electron microscopy (STEM) tomography was the same as described for TEM. Additional sample preparation steps were conducted as described previously (84, 85). Tomogram acquisition was conducted on a STEM Jeol JEM-2100F with an acceleration voltage of 200 kV. Tilt series were acquired from 600 nm thin sections from +72° to -72° with a 1.5° increment using the bright field detector. Image series were reconstructed to tomograms by weighted back projection with the IMOD software package (86). 3D visualization of the membrane structures was performed using Avizo lite software (Visualization Science Group, Burlington, MA, USA) by threshold segmentation.

Western blotting. Western blotting procedures, including primary and secondary antibodies used for detection of HA tag, UL148, ATF4, eIF2α, P-eIF2α (Ser51), the HCMV viral nuclear antigen IE1, and the conditions used for detection of Ser51 phosphorylated eIF2α, were carried out as described previously (8, 10). Additional antibodies used in this study were mouse anti-GAPDH (Cat. No. 60004-1, Proteintech, Rosemont, IL,), mouse anti-gB clone 27-180 (87) (a generous gift of William J. Britt), and anti-GFP (D5.1) XP® Rabbit mAb #2956 (Cell Signaling Technology, Danvers, MA).

824 **Solubility analyses.** 2.0×10^5 human fibroblasts were infected at an MOI of 1 $TCID_{50}$
825 per cell with TB_148^{HA} or TB_159^{HA}. The following day, cells were washed twice with
826 PBS to remove viral inoculum and replenished with DMEM containing 5% newborn calf
827 serum. At the indicated times post-infection, cells were washed once with PBS and
828 lysed by direct addition of 100 μL RIPA buffer [25 mM HEPES (pH 7.5), 400 mM NaCl,
829 0.1% SDS, 0.5% sodium deoxycholate, 1% NP-40, supplemented with 1× protease
830 inhibitor cocktail (ApexBio)]. Lysates were collected and rotated at 4˚C for 1 h.
831 Insoluble material was pelleted by centrifugation (21,000 × *g*, 35 min). Supernatants
832 containing soluble material were transferred to a fresh microfuge tube, and 33 μL of 4×
833 Laemmli sample buffer [200 mM Tris (pH 6.8), 8% SDS, 40% glycerol, 0.08%
834 bromophenol blue] was added to bring final volume to 133 μL. The pellet was disrupted
835 in 133 μL of 1X Laemmli buffer prepared by diluting 4× Laemmli buffer in RIPA buffer.
836 Samples were reduced by addition of beta-mercaptoethanol (5% final, v/v) and boiled at
837 90˚C for 10 min. 40 μL of each sample was resolved by SDS-PAGE (12%
838 polyacrylamide gel), transferred overnight to nitrocellulose membrane, and
839 immunoblotted with antibodies against HA epitope or HCMV gB. Quantitation of
840 secondary antibody fluorescence signals were performed using an Odyssey CLx
841 scanner (Li-Cor, Inc., Lincoln, NE) in auto-scan mode. For each time-point, the signals
842 from RIPA-soluble and insoluble bands were summed to yield total signal, and the ratio
843 of insoluble band signal to total signal were also reported as percent insoluble HA over
844 total HA signal.
845

Statistical analyses. Statistical analyses were carried out using GraphPad Prism 8.1.0 for MacOS (GraphPad, Inc., San Diego, CA).

ACKNOWLEDGEMENTS.

This project was supported by NIH grants R01-AI116851 (to J.P.K.) and P30-GM110703. Its contents are solely the responsibility of the authors and do not necessarily represent the official views of the NIAID or the NIGMS.

We are especially grateful to Erik L. Snapp (HHMI, Janelia Laboratories) for helpful discussions and detailed advice on interpretation of EM and confocal image data concerning the nature of the UL148-dependent ER structures. We also thank Dong Yu (Washington University, St. Louis, MO, currently GSK Vaccines), Thomas E. Shenk (Princeton University, Princeton, NJ), Richard J. Stanton (Cardiff University, United Kingdom), William J. Britt (University of Alabama, Birmingham), W. L. William Chang and Peter A. Barry (both of the University of California, Davis; Davis, CA), Christian Sinzger (University Medical Center Ulm, Ulm, Germany), Klaus Früh (Oregon Health Sciences University, Beaverton, OR), and Gregory A. Smith (Northwestern University, Chicago, IL) for generously sharing reagents.

AUTHOR CONTRIBUTIONS.

Performed experiments: HZ, CR, CCN, MNAS, JvE. Data analysis and interpretation: HZ, CR, CCN, JvE, CS, JPK. Designed experiments: HZ, CR, CCN, JvE, and JPK. Contributed new reagents: HZ, CH, CCN, JPK. Electron microscopy and STEM

868 tomography: CR and JvE. Protein solubility analyses: CCN. Obtained funding: JPK.
869 Wrote the manuscript: JPK with comments from JvE and CR.

870 HZ performed all confocal immunofluorescence experiments with the exception of
871 those shown in SI Figure S1D, which were carried out by JvE. HZ also carried out the
872 viral replication kinetics experiments and constructed novel plasmids, including the
873 lentivirus vectors used to isolating i148^{GFP} and i159^{GFP} ARPE-19 cell populations. HZ also
874 carried out FRAP studies, performed all live cell imaging studies, and all Western blots in
875 the study, except those otherwise specified below. CR carried out the TEM and STEM
876 tomography studies. CCN constructed the TB_159^{HA} virus and conceived of and
877 performed the protein solubility analyses comparing UL148 and Rh159. MS carried out
878 the Western blotting studies on the effects of folimycin versus epoxomicin on UL148
879 degradation. CH designed and carried out the strategy to incorporate an HA-tag at the C-
880 terminus of *Rh159* in RhCMV 68-1. JPK and CN designed the strategies to construct all
881 other new plasmids and recombinant BACs for the study; CN also designed and carried
882 out the strategy to construct TB_159^{HA}. CS assisted with confocal imaging and with
883 Imaris and Nikon software analyses of the 3D images.
884
885
886
887
888
889
890
891

FIGURES.

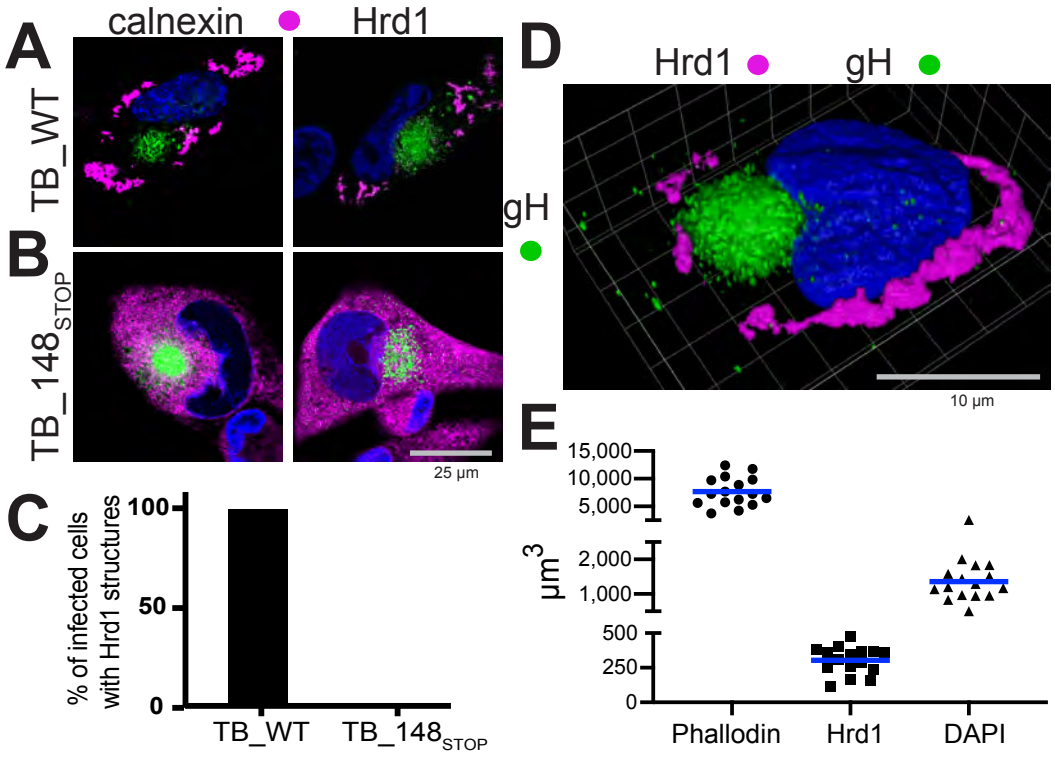

FIG 1. UL148 reorganizes ER markers into anomalous structures during HCMV infection.
Fibroblasts infected at 1 MOI with either **(A)** wildtype HCMV strain TB40/E (TB_WT) or **(B)** an isogenic *UL148*-null mutant (TB_148$_{STOP}$), were fixed at 96 h postinfection (hpi) and imaged by confocal microscopy after staining with antibodies specific for calnexin or Hrd1 (magenta) and glycoprotein H (gH, green), as indicated. DAPI (blue) signal was used to counterstain nuclei. **(C)** Percentage of fibroblasts that contain Hrd1 structures at 96 hpi; fifty gH-positive cells for each condition were scored for the presence or absence of UL148 structures (also see SI Fig S1A). (**D**) 3D confocal image projection of a TB_WT infected fibroblast stained at 96 hpi for Hrd1 and gH. **(E)** Volumetric measurements were made from sixteen infected cells, stained with phalloidin-AlexaFluor 594 conjugate to estimate total cell volume, with Hrd1 antibody to estimate the volume of UL148-dependent ER structures, and with DAPI to estimate nuclear volume.

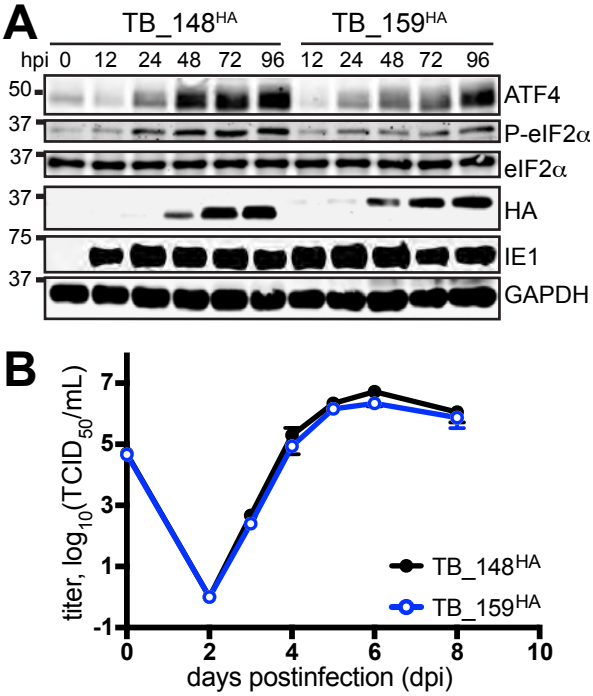

FIG 2. Characterization of TB_148^{HA} and TB_159^{HA} viruses. **(A)** Human fibroblasts were infected at MOI 1 with the indicated recombinant HCMVs and whole cell lysate samples harvested at the indicated times post-infection (h post-infection: hpi) were analyzed by Western blot to detect HA-tagged UL148 or Rh159, the 72 kD viral nuclear antigen IE1-72 (IE1), and GAPDH. **(B)** Single-cycle viral replication kinetic curves from MOI 1 infected fibroblasts were plotted by determining the titer in tissue culture infectious dose 50 ($TCID_{50}$) from supernatants collected at the indicated times postinfection.

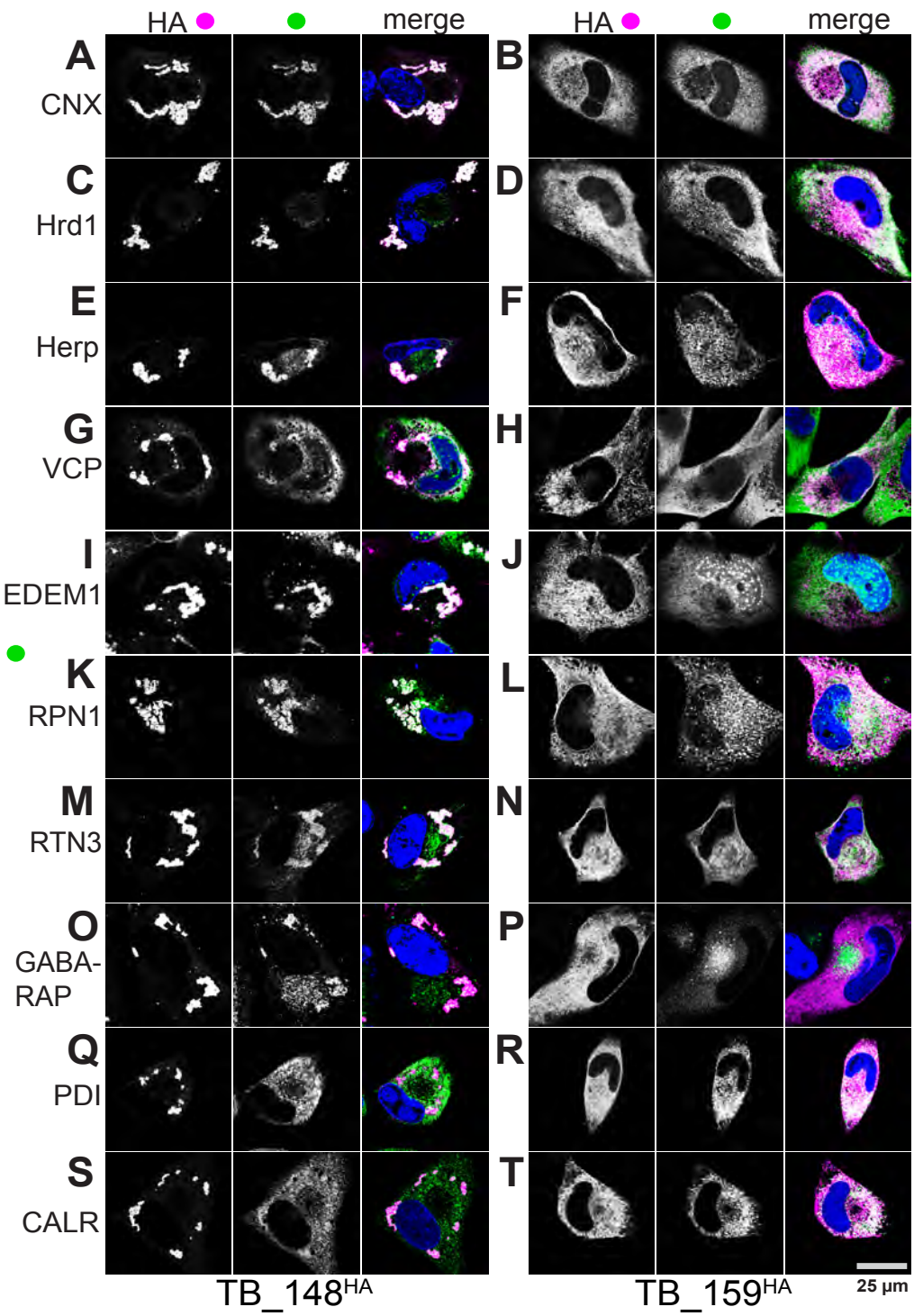

FIG 3. UL148 localizes to unusual ER compartments that are enriched for glycoprotein quality control markers. Fibroblasts infected at MOI 1 with either TB_148^{HA} (panels: **A, C, E, G, I, K, M, O, Q, S**) or TB_ 159^{HA} (panels: **B, D, F, H, J, L, N, P, R, T**) were fixed at 96 h postinfection, and imaged by confocal microscopy after co-staining with antibodies specific for HA (UL148 / Rh159, magenta in merge) and the indicated cellular markers (green in merge). DAPI (blue) counterstaining is shown in merged image.

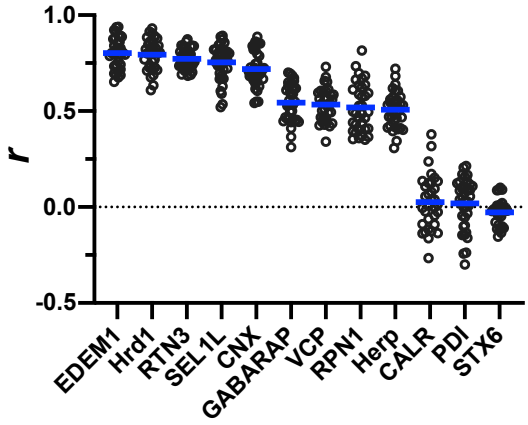

FIG 4. Quantification of co-localization between UL148 and cellular markers. A Pearson's correlation coefficient (*r*) was calculated using NIH ImageJ software to estimate the degree of co-localization between UL148 (HA signal) and each of the indicated cellular markers. A minimum of 30 cells were analyzed per marker. The arithmetic mean for each co-localization analysis result is shown as a blue line, and data points for individual cells analyzed are plotted as circles.

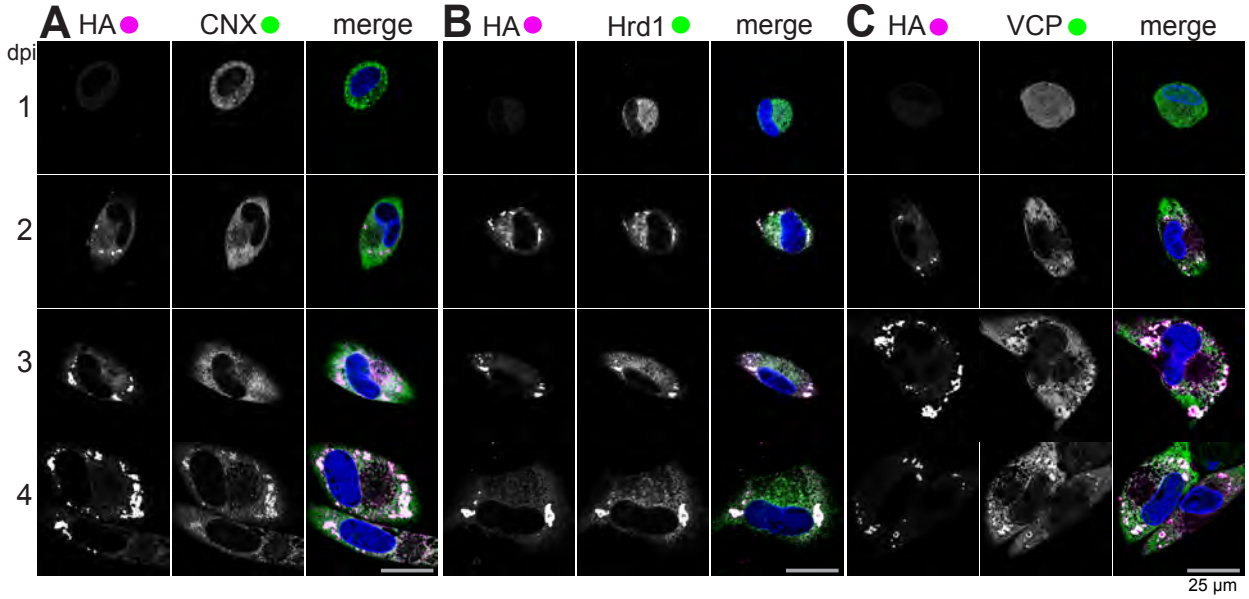

FIG 5. Cellular proteins involved in glycoprotein quality control are recruited with differing kinetics to UL148 ER structures. Fibroblasts infected with TB_148^{HA} at 1 MOI were fixed at the indicated time points (days post infection, dpi) and imaged by confocal microscopy after staining with antibodies specific for HA (UL148, magenta), CNX (green, **A**) , Hrd1 (green, **B**) or VCP(green, **C**), DAPI (blue).

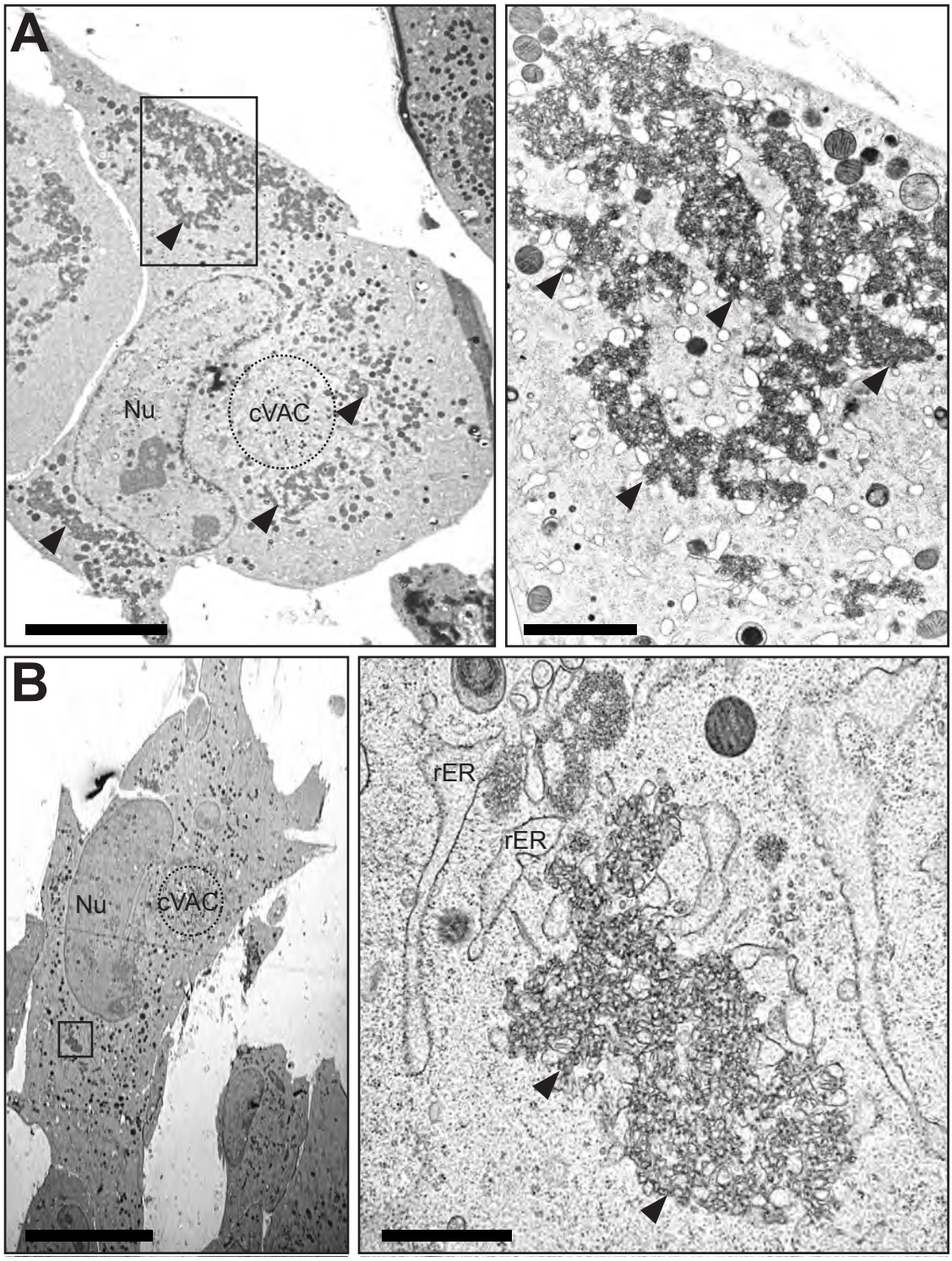

FIG 6. TEM of ER structures in wild-type HCMV infected cells. Human fibroblasts infected with wildtype HCMV (TB_WT) were fixed by high-pressure freezing and freeze substitution at day 5 postinfection and imaged using TEM. Panels (**A**) and (**B**) show cell overview at left. For each cell, the boxed region is shown at higher magnification. Scale bars; left panels: 10 μm, right panels: 2 μm. rER: rough ER; Nu: nucleus; cVAC: cytoplasmic viral assembly compartment. Solid arrowheads indicate the UL148-dependent ER structures of interest.

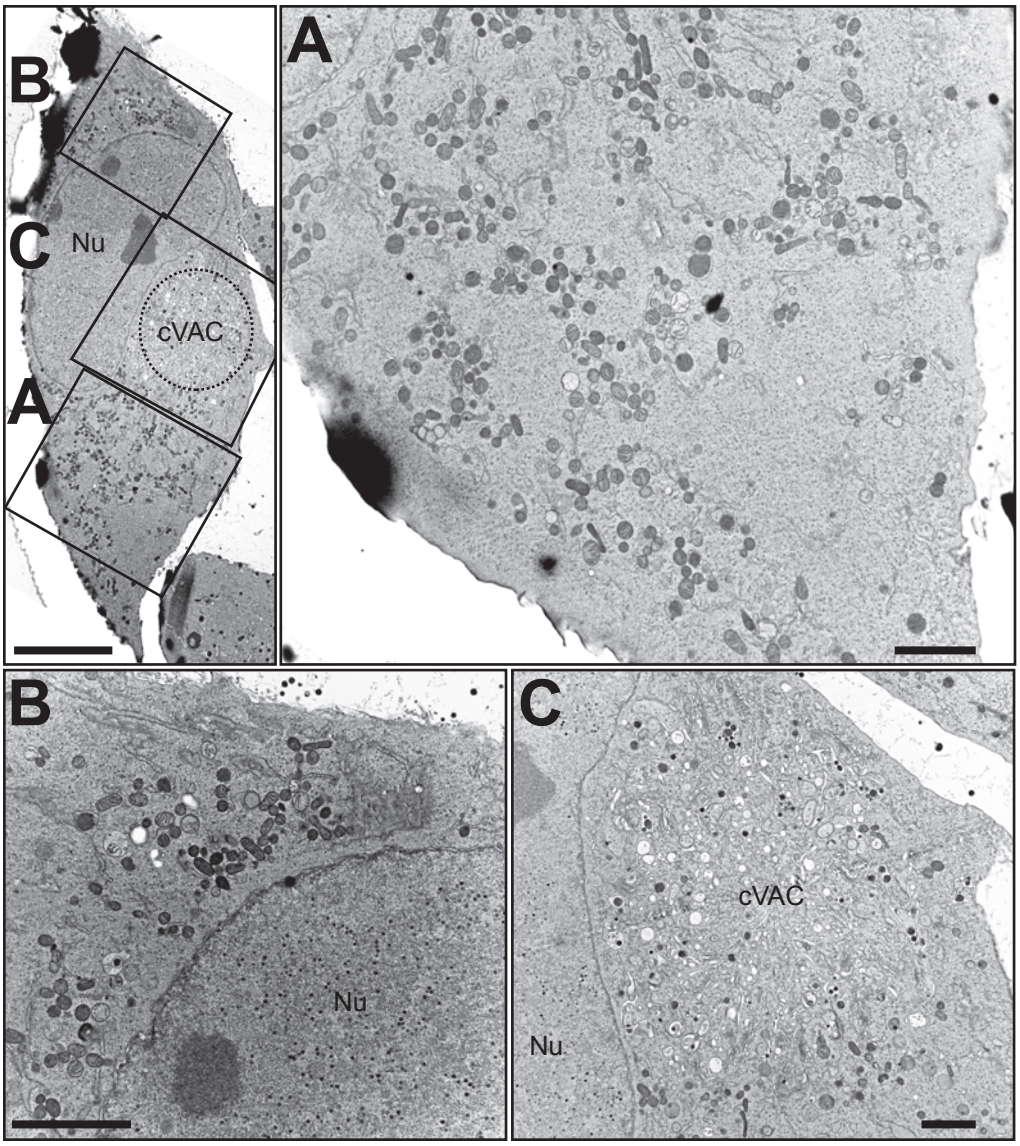

FIG 7. TEM of *UL148*-null HCMV infected cells. Human fibroblasts infected with a *UL148*-null mutant (TB_148$_{STOP}$) were fixed by high-pressure freezing and freeze substitution at day 5 postinfection and imaged using TEM. At the upper left an overview panel of a representative cell is shown with panels (**A)**, **(B)**, and **(C)** each boxed. The boxed regions are expanded at higher magnification at right (**A**) and below (**B, C**). Scale bars for upper left overview panel: 10 μm, for zoomed panels: 2 μm. rER: rough ER; Nu: nucleus; cVAC: cytoplasmic viral assembly compartment.

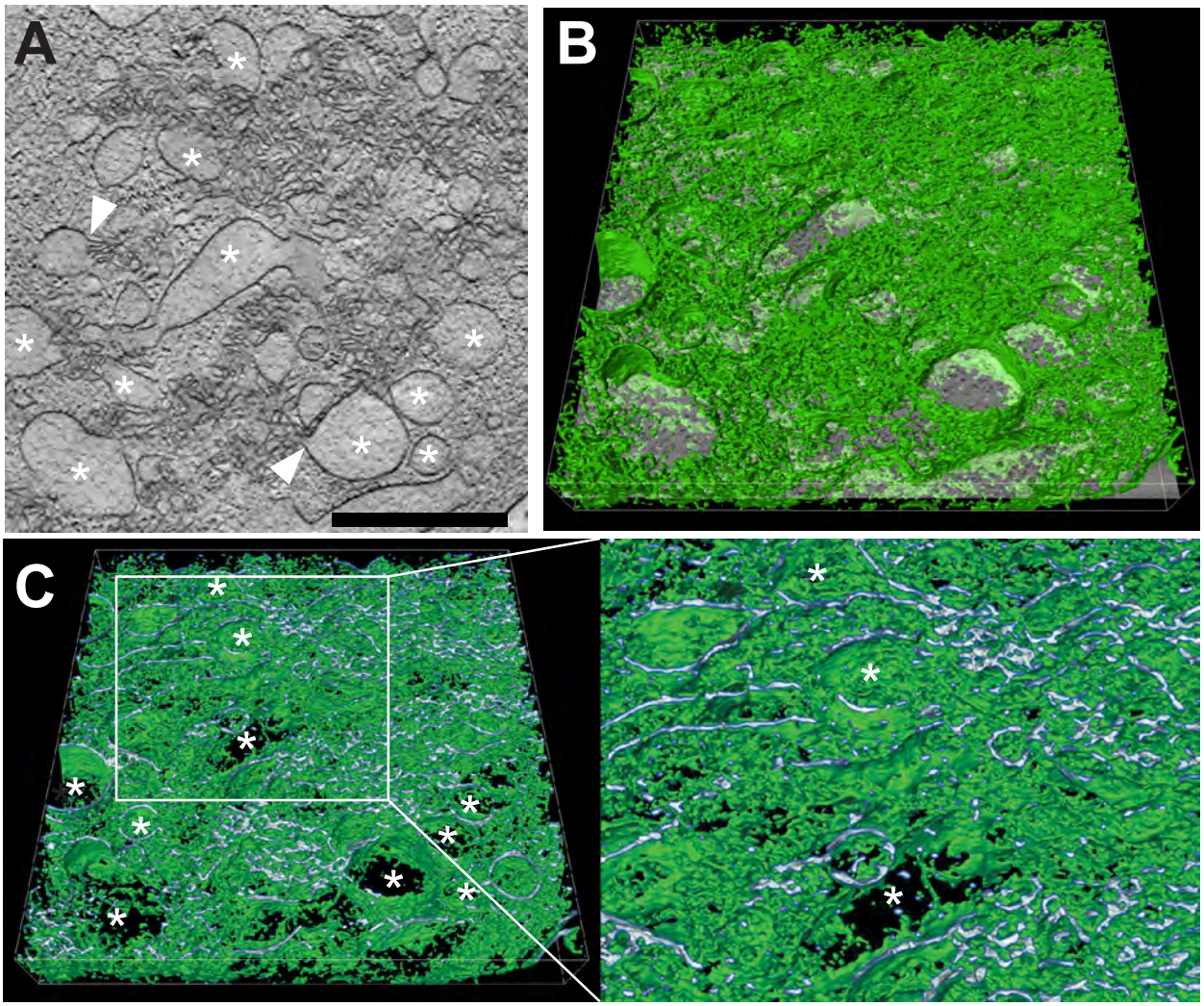

FIG 8. STEM tomography of UL148-dependent ER structures in HCMV infected cells. Human fibroblasts infected with wildtype HCMV (TB_WT) were fixed by high-pressure freezing and freeze substitution at day 5 postinfection and tomograms were recorded by STEM. (**A**) Shows a virtual section through the tomogram of a virus-induced membranous structure; asterisks denote ER structures of distended lumenal space. White arrowheads indicate sites at which membranes originating from distended ER cisternae continue into areas of involuted collapsed ER. Scale bar: 1 µm. (**B**) Shows the same virtual section as in (A) tilted and with a 3D visualization of the membranous network (green) of the entire tomogram. The same distended ER cisternae as in (A) are marked by asterisks. (**C**) Shows a cross section through (B) to visualize the membrane profile of the membranous structures. The region delimited by a white box is shown in a higher magnification on the right. Finer detail of the enlarged ER cisternae and the connections between them are readily visible; asterisks indicate the same distended ER cisternae as in panels (A) and (B). Also, see SI Movie S1. Scale bar: 1 µm.

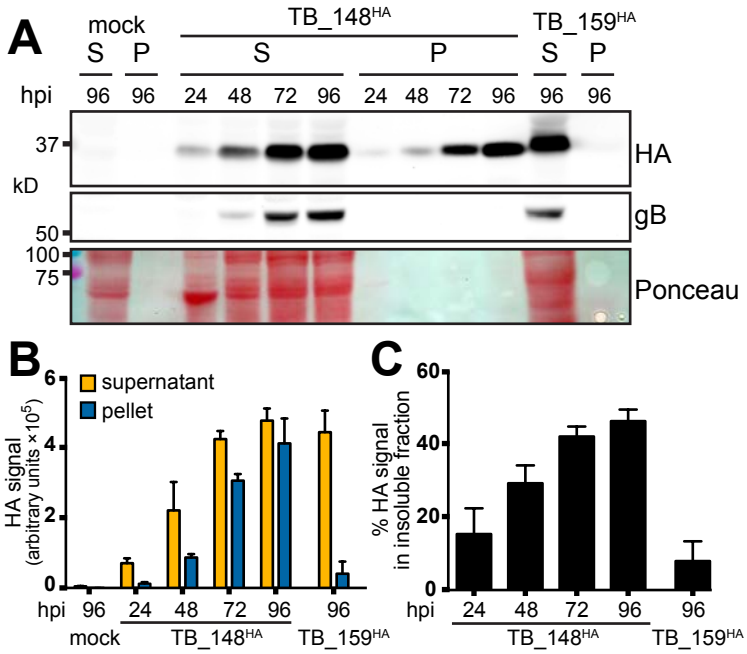

FIG 9. Solubility analysis of UL148 and Rh159. (**A**) Human fibroblasts were infected at MOI 1 $TCID_{50}$/cell with HCMV strain TB40/E derived viruses TB_148^{HA}, which expresses UL148 fused at its C-terminus to an HA-epitope tag, or TB_159^{HA}, which lacks *UL148* and instead expresses rhesus CMV Rh159 carrying a C-terminal HA tag. At the indicated times postinfection (hpi), infected cells were collected radioimmunoprecipitation (RIPA) lysis buffer, centrifuged at 21,000 × *g* for 30 min, after which supernatant (sup) and pellet (pel) fractions were boiled in gel loading buffer containing 2% sodium dodecyl sulfate (SDS). Equivalent portions of supernatant and pellet were resolved by SDS-polyacrylamide gel electrophoresis, transferred to a nitrocellulose membrane for detection of protein species immunoreactive to antibodies against HA epitope (HA) and HCMV glycoprotein B (gB) and for total protein signal using Ponceau S reagent (Ponceau). (**B-C**). Signal intensity of fluorophore-conjugated secondary antibodies in anti-HA Western blots were measured from three independent biological replicates of the experiment shown in (A); error bars indicate standard deviation. (**B**) The fluorescent signal for each infection time point condition (Y-axis indicates arbitrary units, in hundred thousands). (**C**) The amount of signal found in the insoluble (pellet) fraction relative to the total signal (pellet plus supernatant) for each infection time point are plotted as percentage values.

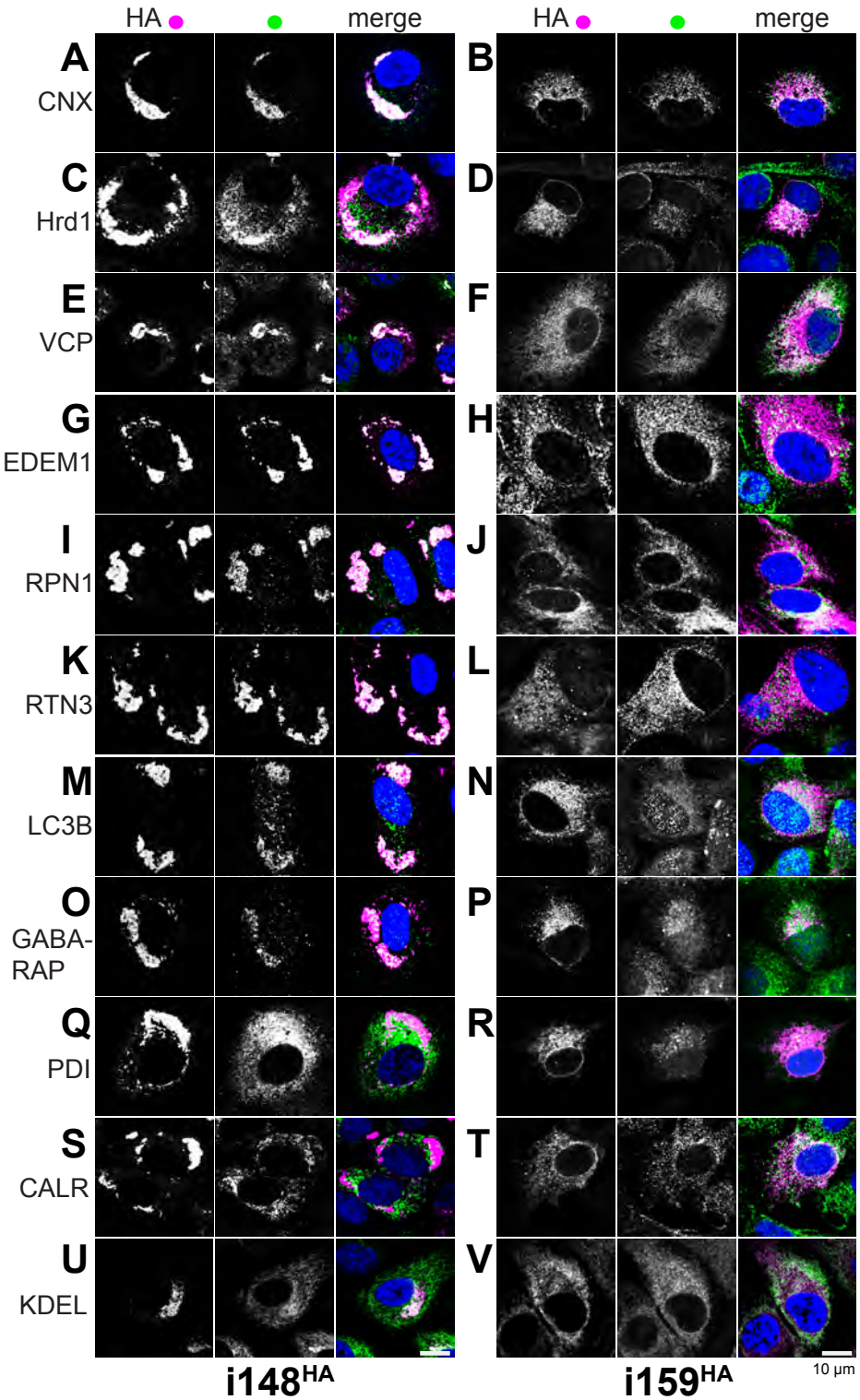

FIG 10. UL148 is sufficient to remodel the ER. HA-tagged UL148 or Rh159 were doxycycline (dox) induced in the context of a "tet-on" lentiviral vector system in stably transduced ARPE-19 epithelial cell populations, i148^{HA} and i159^{HA}, respectively. Cells were fixed at 48 h postinduction for indirect immunofluorescence staining for the indicated cellular markers (green) together with HA (magenta). Scale bar: 10 µm.

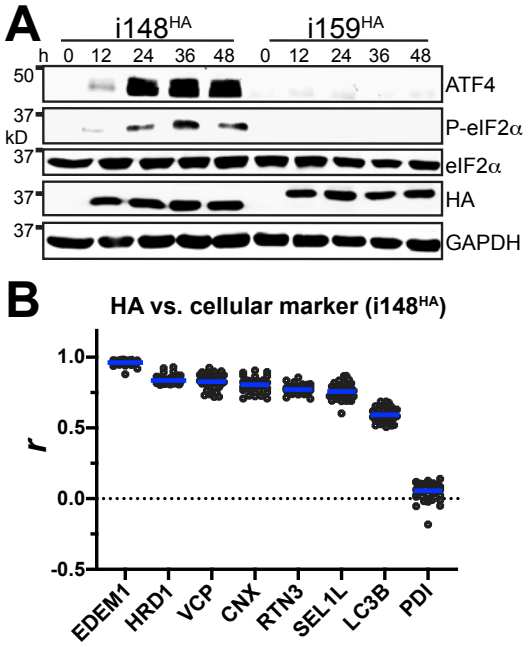

FIG 11. ISR activation accompanies redistribution of ER markers during ectopic expression of UL148. (A) Lysates of tet-on ARPE-19 cells expressing either UL148 or Rh159 fused to an HA tag, $i148^{HA}$ and $i159^{HA}$, respectively, were collected at the indicated times post doxycycline (dox) induction and analyzed by Western blot for the expression of the indicated proteins and for the abundance of eIF2α phosphorylated at Ser51 (P-eIF2α) using a phospho-specific antibody. (**B**) Pearson's correlation coefficient (*r*) values were calculated using NIH ImageJ software estimate the degree of co-localization between UL148 (HA signal) and the indicated cellular markers. A minimum of 30 cells were analyzed per marker. Arithmetic means for each co-localization analysis result are shown as blue lines, and data points for individual cells analyzed are plotted as circles.

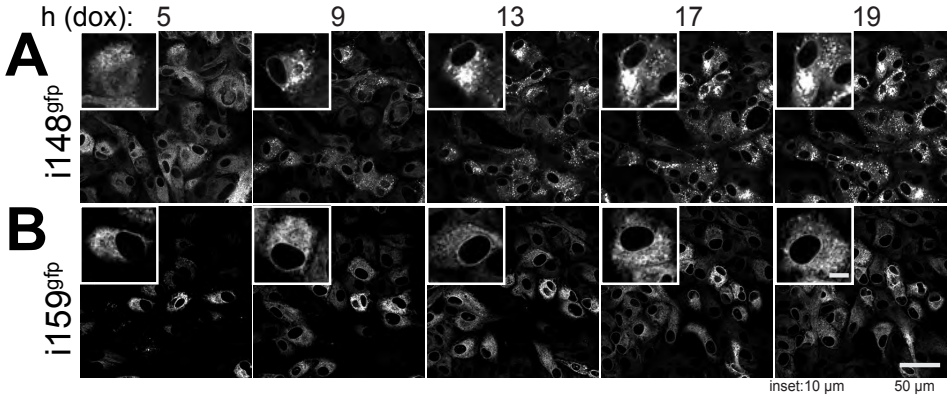

FIG 12. Live-cell Imaging of UL148-GFP and Rh159-GFP during induced ectopic expression. "Tet-on" ARPE-19 epithelial cells that inducibly express either UL148 or Rh159 fused to green florescent protein (gfp), $i148^{gfp}$ (**A**) and $i159^{gfp}$ (**B**), respectively, were induced for transgene expression using 100 ng/mL doxycycline (dox) and imaged using live-cell microscopy. Images from the selected time points (h post treatment with dox, hpt) are shown. The main scale bar represents 50 μm. For inset panels at upper left of each image, which are magnified 2.4× relative to the main image, the scale bar represents 10 μm. Also see SI Movies S2-S3.

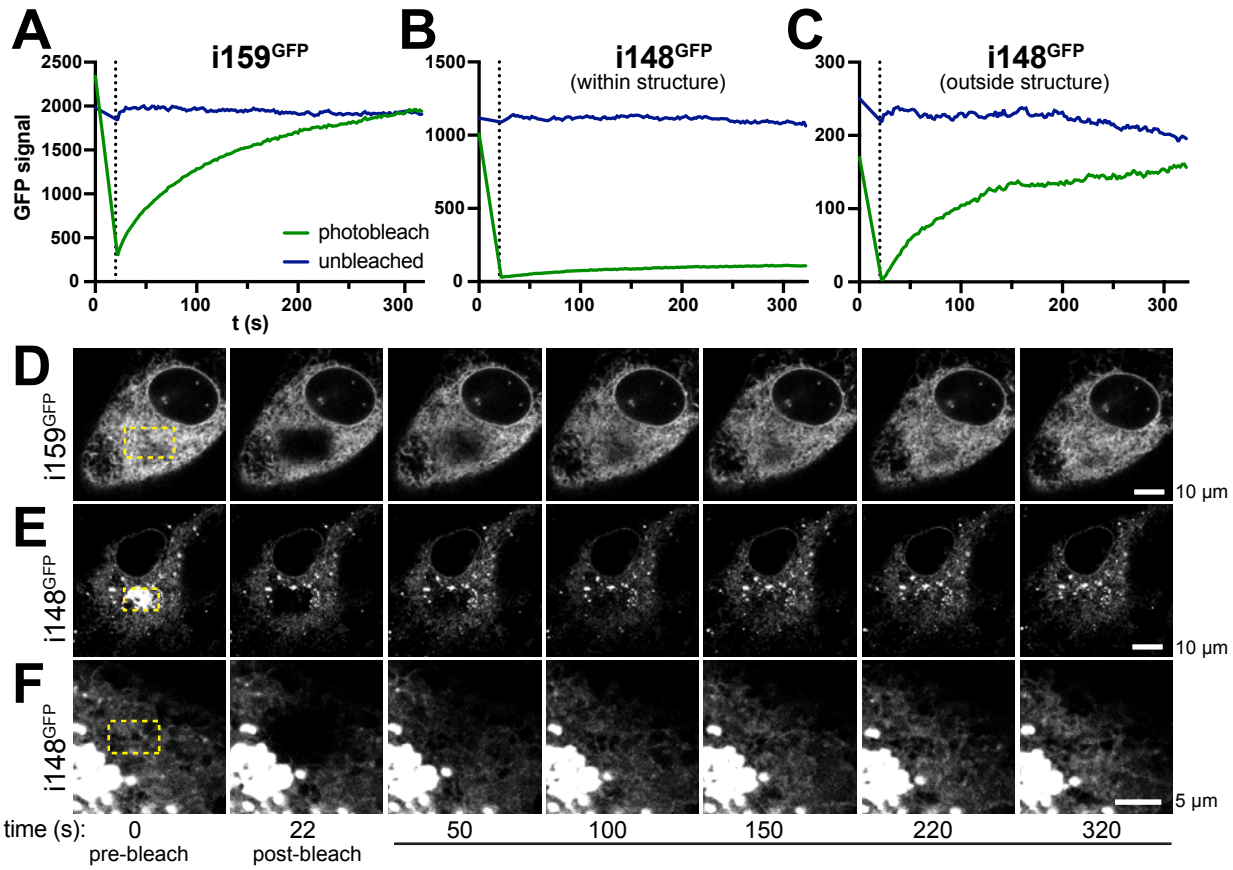

FIG 13. FRAP analysis. ARPE-19 cells that inducibly express Rh159-GFP, i159^{gfp} (**A**) or UL148-GFP, i148^{gfp} (**B-C**) were doxycycline induced for 24 h (100 ng/mL doxycycline (dox). Separate regions of GFP signal in selected cells were photobleached (405 nm laser) or left unbleached, while a third region lacking GFP signal was chosen as a background reference were measured before and during fluorescence recovery after photobleaching (FRAP). Note: background signal was not plotted because values were resolvable from the x-axis. GFP signal intensity is plotted over a time period (seconds, s) starting with an exposure at t=0 (immediately before photobleaching), and including measurements taken every 2 s after photobleaching (0-20 s) until termination of the measurement series at t=322 s (300 s of FRAP). (**D-F**) Images from the selected time points (s, seconds) immediately before and after bleaching, and during fluorescence recovery period. Also see SI Movies S4-S6.

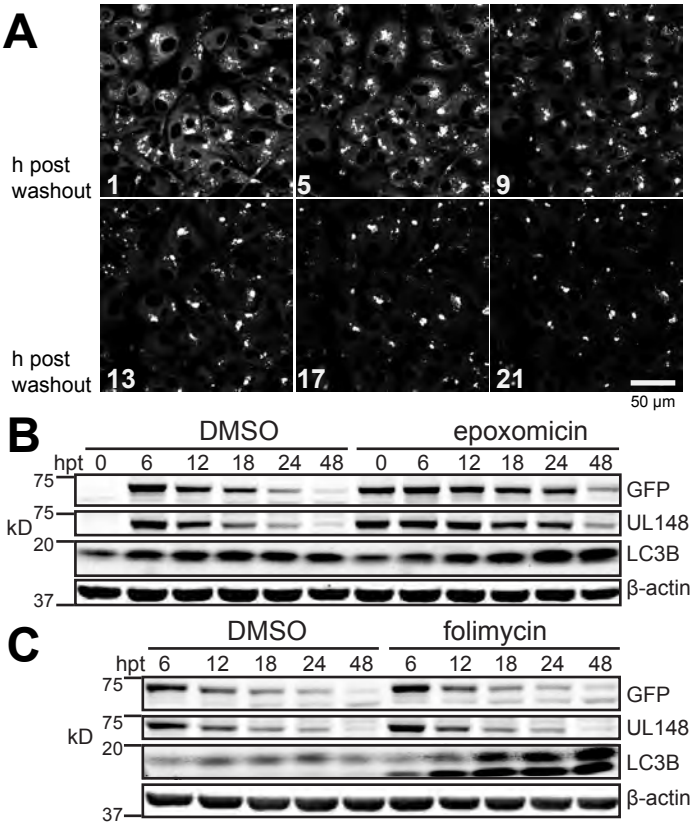

FIG 14: UL148-GFP is stabilized by inhibition of proteasomal but not lysosomal degradation. "Tet-on" ARPE-19 cells that inducibly express UL148-GFP (i148^{gfp}) were induced for 24 h by the addition of 100 ng/mL doxycycline (dox), after which the dox inducing agent was washed out and medium containing either the proteasome inhibitor epoxomicin (20 µM) or the proton pump inhibitor folimycin (115 nM) was added and samples were harvested for Western blot analysis at the indicated times post treatment (h post treatment, hpt) with folimycin or epoxomicin. DMSO was added at 0.1% to control for folimycin, or 1% to control for epoxomicin. Also see SI Movie S7.

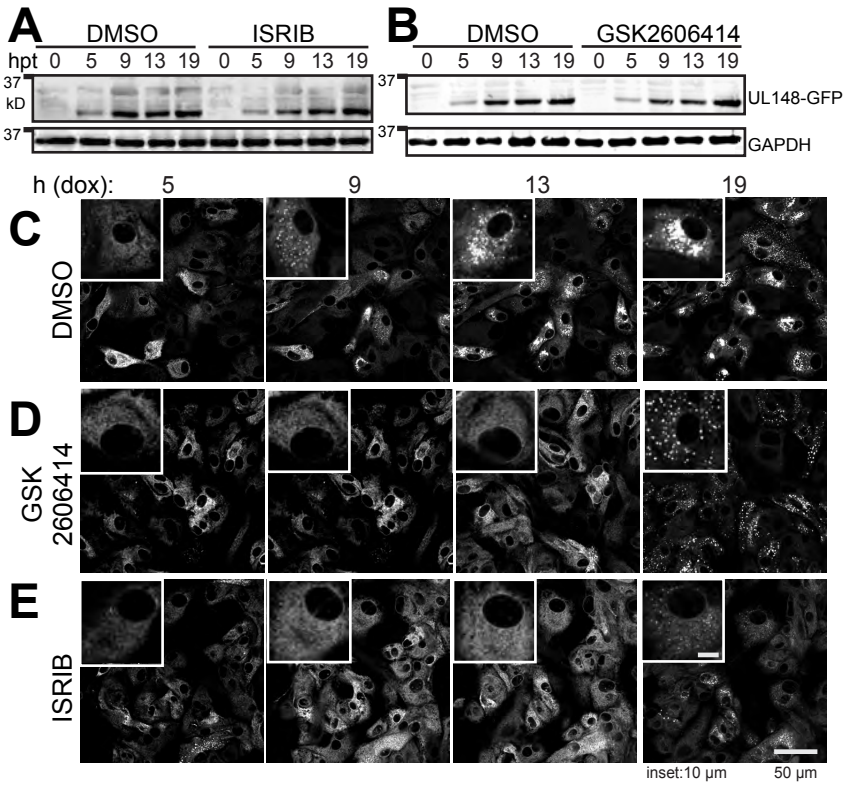

FIG 15. Inhibition of the integrated stress response impedes UL148-mediated ER remodeling. "Tet-on" ARPE-19 epithelial cells that inducibly express either UL148 or Rh159 fused to green florescent protein (gfp), i148^{gfp} (**A**) and i159^{gfp} (**B**), respectively, were induced for transgene expression using 100 ng/mL doxycycline (dox) in the presence of absence of either ISRIB (200 nM) or GSK2606414 (1.1 µM) and monitored by anti-UL148 Western blot for expression of UL148-GFP over a series of time points (h post treatment with dox, hpt). (**C-E**): Live-cell imaging of UL148-GFP and Rh159-GFP expression patterns in the presence of ISRIB (200 nM), GSK2606414 (1.1 µM), or DMSO vehicle (0.01%). Main scale bar represents 50 µm. For inset panels at upper left of each image, which are magnified 2.4× relative to the main image, the scale bar represents 10 µm. Also see SI Movies S8-S10.

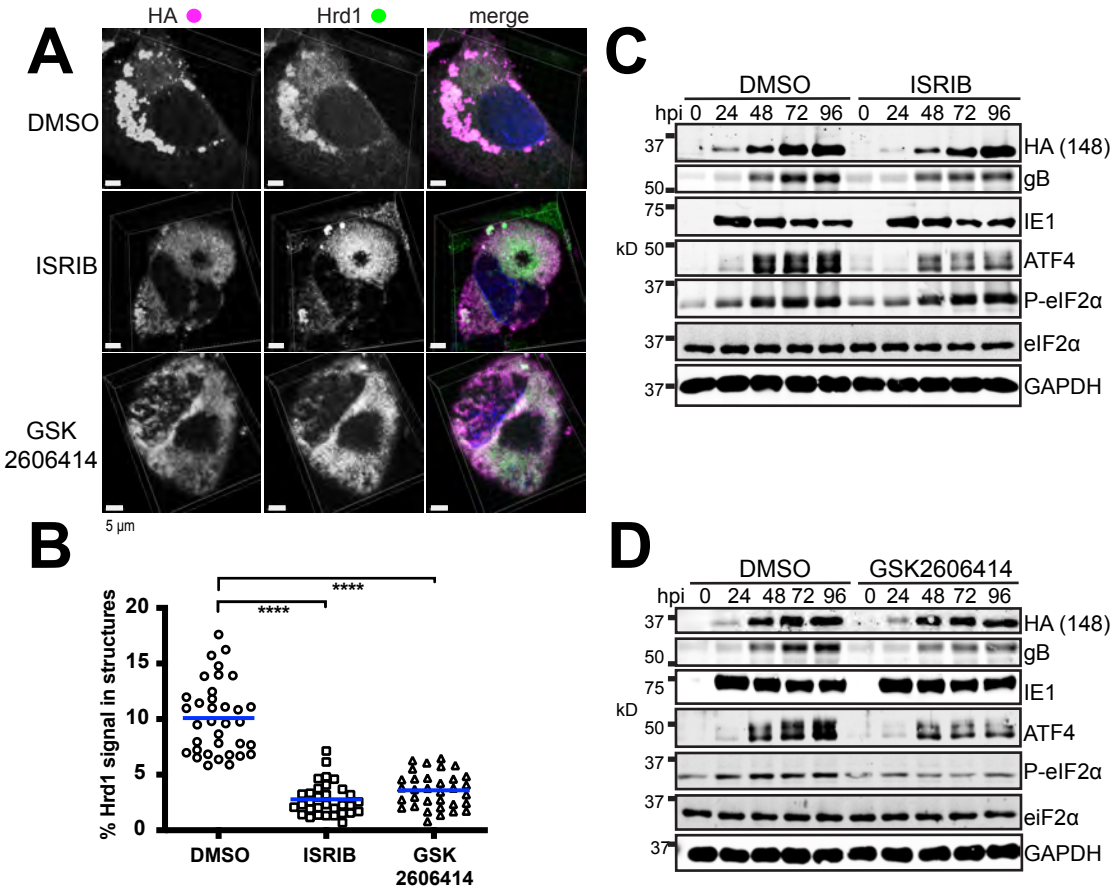

FIG 16. Inhibition of the ISR prevents the coalescence of Hrd1 and UL148 into discrete structures during infection. (**A**) Representative 3D maximum intensity projections of confocal imaging Z-stacks obtained from cells infected at MOI 1 for 96 h with HCMV strain TB40/E carrying an HA-tagged *UL148*, TB_148^{HA}, and maintained in the presence of ISRIB (200 nM), GSK2606414 (1.1 µM), or DMSO carrier alone (0.1% vol/vol). In merged images HA signal is shown in magenta, Hrd1 in green, and DAPI counterstaining in blue. (**B**) The percent of Hrd1 antibody signal involved in discrete structures at 96 hpi were calculated for a minimum of 30 cells per condition were determined using Imaris x64 9.3.0 software. Statistical significance was determined using a one-way ANOVA followed by Tukey's post-test; **** represents a P-value of <0.0001. The arithmetic mean for co-localization analysis results are shown as blue lines with data points for individual cells analyzed plotted as circles, squares or triangles, as indicated. (**C-D**) Western blot analyses of fibroblasts infected at MOI 1 with TB_148^{HA} and maintained in the presence of ISRIB (200 nM), GSK2606414 (1.1 µM), or DMSO carrier alone (0.01%); hpi: h post infection (hpi). Note: a phospho-specific antibody was used for detection of eIF2α phosphorylated at Ser51 (P-eIF2α).

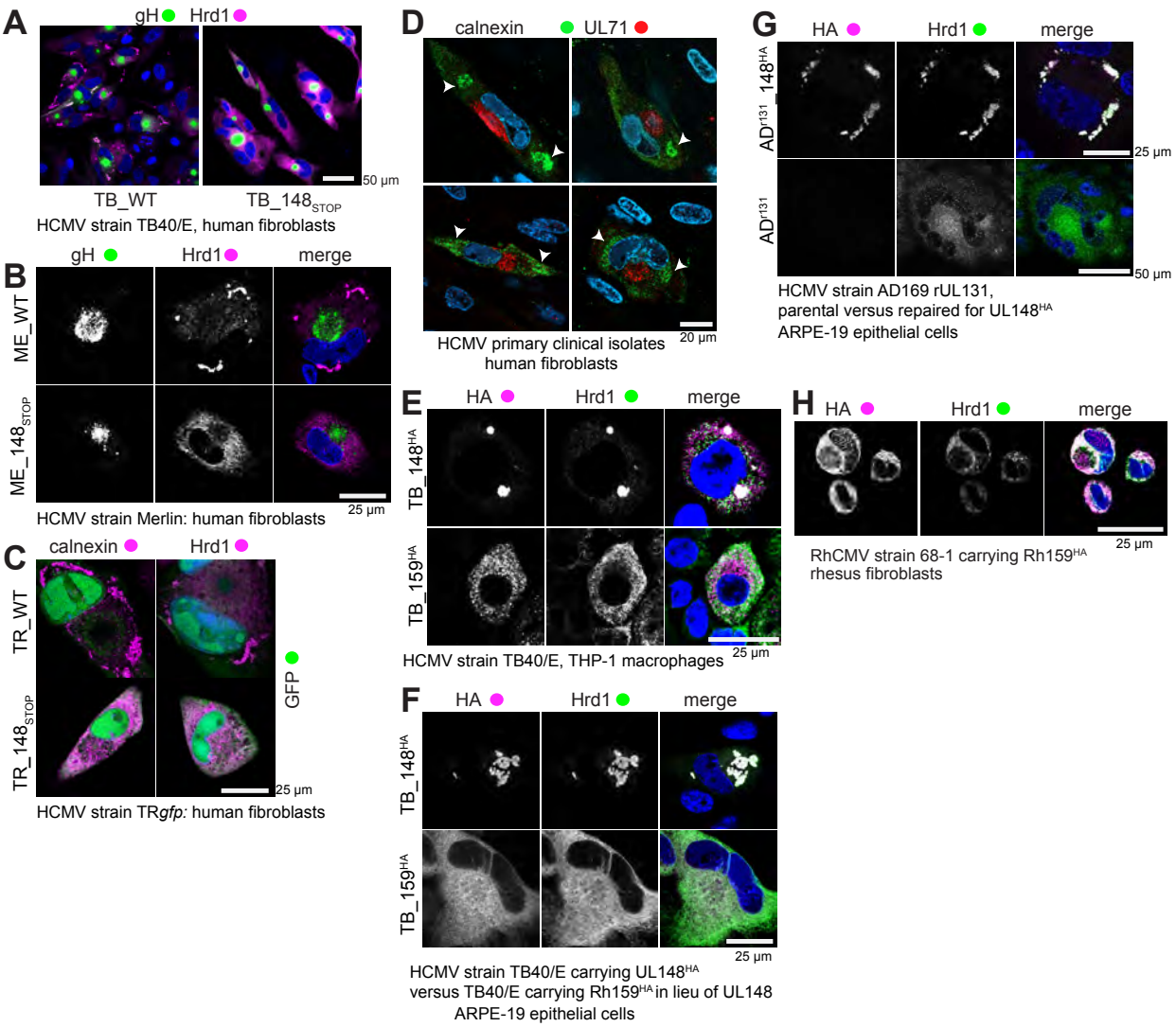

FIG S1: **Additional indirect immunofluorescent confocal microscopy results from infected cells.** (**A**) Lower magnification overview of results from FIGS 1A-B; staining of HCMV glycoprotein H (gH) and Hrd1 at 96 h postinfection (hpi) of human fibroblasts with wildtype HCMV strain TB40/E (WT) versus *UL148*-null derivative TB_148$_{STOP}$. (**B**) Staining of gH and Hrd1 at 96 hpi of human fibroblasts with wildtype Merlin recovered from BAC-cloned Merlin pAL1393 (ME_WT) or a *UL148*-null derivative of the same virus (ME_148$_{STOP}$.) (**C**): Staining of gH and Hrd1 at 96 hpi of human fibroblasts with wildtype HCMV strain TRgfp recovered from BAC-cloned TRgfp (TR_WT) or a *UL148*-null derivative of the same virus (TR_148$_{STOP}$). (**D**) Staining of the viral tegument protein UL71 and calnexin 5 days postinfection of human fibroblasts with primary clinical HCMV isolates obtained from patient throat swabs. (**E**) Staining against HA and Hrd1 in THP-1 macrophages fixed at 96 hpi with HCMV strain TB40/E derivative viruses TB_148^{HA} or TB_159^{HA}; note: THP-1 monocytes were differentiated using phorbol ester treatment. (**F**) Staining of HA and Hrd1 in ARPE-19 epithelial cells infected for 96 h with either TB_148^{HA} or TB_159^{HA}. (**G**) Staining of HA and Hrd1 in ARPE-19 epithelial cells infected for 96 h with HCMV strain AD169 repaired for *UL131* and to which an HA-tagged UL148 CDS from TB40/E was restored to the native *UL148* locus (AD^{r131}_148^{HA}) or with a parental AD169 virus repaired for *UL131* to which *UL148* was not restored (AD^{r131}). Notes: (i) a functional *UL131* is required for efficient infection of epithelial cells; (ii) for ADr131 we did not employ a viral marker (e.g., HA) to identify infected cells, so the appearance of syncytia and the characteristic kidney-bean shaped nucleus was used to indicate infected cells and a slightly lower magnification was used to best show these features, hence a different scale bar was used. (**H**) Staining for HA and Hrd1 in telomerase-immortalized rhesus fibroblasts infected with BAC-derived rhesus CMV (RhCMV) strain 68-1 carrying an HA-tag at the C-terminus of Rh159.

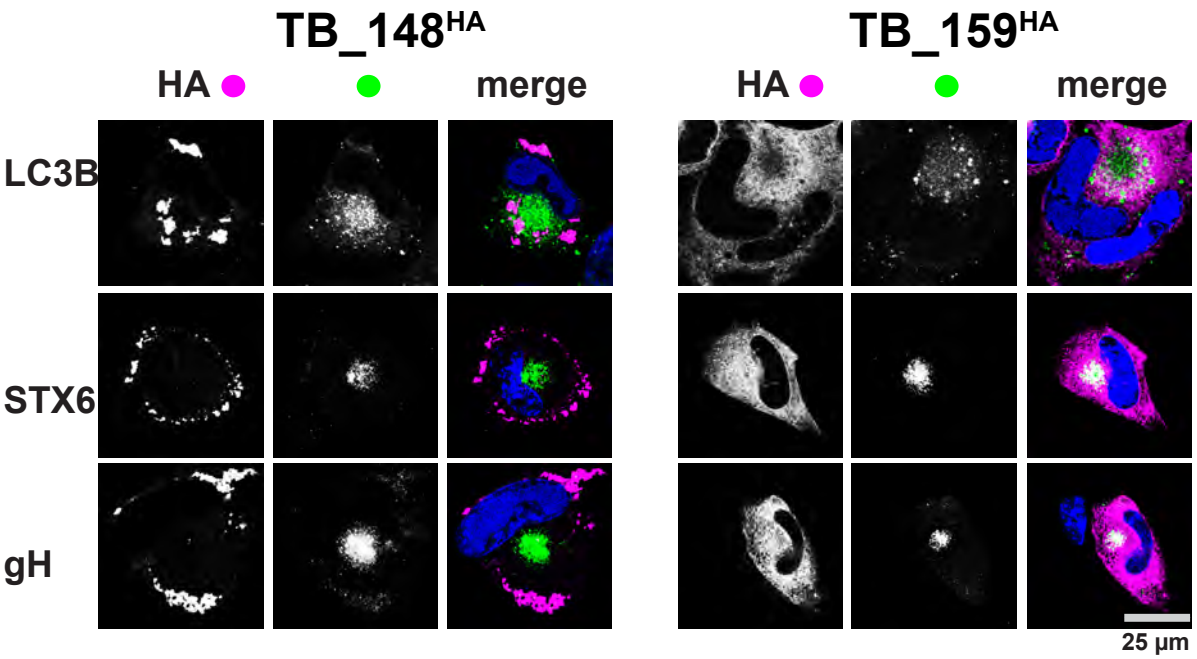

FIG S2: Confocal microscopy of LC3B, syntaxin-6 and glycoprotein H staining during HCMV infection. Human fibroblasts were infected with the indicated viruses for 96 h and then fixed, permeabilized, and stained using antibodies specific for the indicated proteins. Indirect immunofluorescence images were captured using a 63X objective on a Leica SP5 confocal microscope. gH: glycoprotein H, STX6: syntaxin-6.

SUPPLEMENTARY VIDEO FILES.

Movie S1: STEM tomography of anomalous ER structures in wildtype HCMV infected fibroblasts at day 5 postinfection.

Movies S2 – S3: Live cell imaging of GFP signal following dox induction of transgene expression in i148^{gfp} and i159^{gfp} ARPE-19 epithelial cells.
Movie S2: i148^{gfp} cells from 2-19 h post dox induction.
Movie S3: i159^{gfp} cells from 2-19 h post dox induction.

Movies S4-S6: FRAP.
Movie S4: FRAP of UL148-GFP structure (ER within structure)
Movie S5: FRAP of UL148 GFP structure (ER outside structure)
Movie S6: FRAP of Rh159-GFP.

Movie S7: Imaging of UL148-GFP following washout of doxycycline (dox) up to 21 h 37 min post washout of dox.

Movies S8-S10: ISR blockade.
Movie S8: i148^{gfp} cells in the presence of 0.01% DMSO, from 2-19 h post dox induction.
Movie S9: i148^{gfp} cells in the presence of 1.1 µM GSK2606414, from 2-19 h post dox induction.
Movie S10: i148^{gfp} cells in the presence of 200 nM ISRIB, from 2-19 h post dox induction.

REFERENCES.

1. Li G, Nguyen CC, Ryckman BJ, Britt WJ, Kamil JP. 2015. A viral regulator of glycoprotein complexes contributes to human cytomegalovirus cell tropism. Proc Natl Acad Sci U S A 112:4471-6.
2. Wille PT, Knoche AJ, Nelson JA, Jarvis MA, Johnson DC. 2010. A human cytomegalovirus gO-null mutant fails to incorporate gH/gL into the virion envelope and is unable to enter fibroblasts and epithelial and endothelial cells. J Virol 84:2585-96.
3. Jiang XJ, Adler B, Sampaio KL, Digel M, Jahn G, Ettischer N, Stierhof YD, Scrivano L, Koszinowski U, Mach M, Sinzger C. 2008. UL74 of human cytomegalovirus contributes to virus release by promoting secondary envelopment of virions. J Virol 82:2802-12.
4. Zhou M, Lanchy JM, Ryckman BJ. 2015. Human Cytomegalovirus gH/gL/gO Promotes the Fusion Step of Entry into All Cell Types, whereas gH/gL/UL128-131 Broadens Virus Tropism through a Distinct Mechanism. J Virol 89:8999-9009.
5. Wu Y, Prager A, Boos S, Resch M, Brizic I, Mach M, Wildner S, Scrivano L, Adler B. 2017. Human cytomegalovirus glycoprotein complex gH/gL/gO uses PDGFR-alpha as a key for entry. PLoS Pathog 13:e1006281.
6. Kabanova A, Marcandalli J, Zhou T, Bianchi S, Baxa U, Tsybovsky Y, Lilleri D, Silacci-Fregni C, Foglierini M, Fernandez-Rodriguez BM, Druz A, Zhang B, Geiger R, Pagani M, Sallusto F, Kwong PD, Corti D, Lanzavecchia A, Perez L. 2016. Platelet-derived growth factor-alpha receptor is the cellular receptor for human cytomegalovirus gHgLgO trimer. Nat Microbiol 1:16082.
7. Wu K, Oberstein A, Wang W, Shenk T. 2018. Role of PDGF receptor-alpha during human cytomegalovirus entry into fibroblasts. Proc Natl Acad Sci U S A doi:10.1073/pnas.1806305115.
8. Nguyen CC, Siddiquey MNA, Zhang H, Li G, Kamil JP. 2018. Human Cytomegalovirus Tropism Modulator UL148 Interacts with SEL1L, a Cellular Factor That Governs Endoplasmic Reticulum-Associated Degradation of the Viral Envelope Glycoprotein gO. J Virol 92:e00688-18.
9. Wang ECY, Pjechova M, Nightingale K, Vlahava VM, Patel M, Ruckova E, Forbes SK, Nobre L, Antrobus R, Roberts D, Fielding CA, Seirafian S, Davies J, Murrell I, Lau B, Wilkie GS, Suarez NM, Stanton RJ, Vojtesek B, Davison A, Lehner PJ, Weekes MP, Wilkinson GWG, Tomasec P. 2018. Suppression of costimulation by human cytomegalovirus promotes evasion of cellular immune defenses. Proc Natl Acad Sci U S A 115:4998-5003.
10. Siddiquey MNA, Zhang H, Nguyen CC, Domma AJ, Kamil JP. 2018. The Human Cytomegalovirus Endoplasmic Reticulum-Resident Glycoprotein UL148 Activates the Unfolded Protein Response. J Virol 92:e00896-18.
11. Das S, Vasanji A, Pellett PE. 2007. Three-dimensional structure of the human cytomegalovirus cytoplasmic virion assembly complex includes a reoriented secretory apparatus. J Virol 81:11861-9.
12. Sanchez V, Greis KD, Sztul E, Britt WJ. 2000. Accumulation of virion tegument and envelope proteins in a stable cytoplasmic compartment during human cytomegalovirus replication: characterization of a potential site of virus assembly. J Virol 74:975-86.

13. Lilley BN, Ploegh HL. 2005. Multiprotein complexes that link dislocation, ubiquitination, and extraction of misfolded proteins from the endoplasmic reticulum membrane. Proc Natl Acad Sci U S A 102:14296-301.
14. Kamhi-Nesher S, Shenkman M, Tolchinsky S, Fromm SV, Ehrlich R, Lederkremer GZ. 2001. A novel quality control compartment derived from the endoplasmic reticulum. Mol Biol Cell 12:1711-23.
15. Leitman J, Shenkman M, Gofman Y, Shtern NO, Ben-Tal N, Hendershot LM, Lederkremer GZ. 2014. Herp coordinates compartmentalization and recruitment of HRD1 and misfolded proteins for ERAD. Mol Biol Cell 25:1050-60.
16. Houck SA, Ren HY, Madden VJ, Bonner JN, Conlin MP, Janovick JA, Conn PM, Cyr DM. 2014. Quality control autophagy degrades soluble ERAD-resistant conformers of the misfolded membrane protein GnRHR. Mol Cell 54:166-179.
17. Sturgill ER, Malouli D, Hansen SG, Burwitz BJ, Seo S, Schneider CL, Womack JL, Verweij MC, Ventura AB, Bhusari A, Jeffries KM, Legasse AW, Axthelm MK, Hudson AW, Sacha JB, Picker LJ, Fruh K. 2016. Natural Killer Cell Evasion Is Essential for Infection by Rhesus Cytomegalovirus. PLoS Pathog 12:e1005868.
18. Chaumorcel M, Souquere S, Pierron G, Codogno P, Esclatine A. 2008. Human cytomegalovirus controls a new autophagy-dependent cellular antiviral defense mechanism. Autophagy 4:46-53.
19. Chaumorcel M, Lussignol M, Mouna L, Cavignac Y, Fahie K, Cotte-Laffitte J, Geballe A, Brune W, Beau I, Codogno P, Esclatine A. 2012. The human cytomegalovirus protein TRS1 inhibits autophagy via its interaction with Beclin 1. J Virol 86:2571-84.
20. Alwine JC. 2012. The human cytomegalovirus assembly compartment: a masterpiece of viral manipulation of cellular processes that facilitates assembly and egress. PLoS Pathog 8:e1002878.
21. Das S, Pellett PE. 2011. Spatial relationships between markers for secretory and endosomal machinery in human cytomegalovirus-infected cells versus those in uninfected cells. J Virol 85:5864-79.
22. Leitman J, Ron E, Ogen-Shtern N, Lederkremer GZ. 2013. Compartmentalization of endoplasmic reticulum quality control and ER-associated degradation factors. DNA Cell Biol 32:2-7.
23. Cox DW, Billingsley GD, Callahan JW. 1986. Aggregation of plasma Z type alpha 1-antitrypsin suggests basic defect for the deficiency. FEBS Lett 205:255-60.
24. Le A, Ferrell GA, Dishon DS, Le QQ, Sifers RN. 1992. Soluble aggregates of the human PiZ alpha 1-antitrypsin variant are degraded within the endoplasmic reticulum by a mechanism sensitive to inhibitors of protein synthesis. J Biol Chem 267:1072-80.
25. Lomas DA, Evans DL, Finch JT, Carrell RW. 1992. The mechanism of Z alpha 1-antitrypsin accumulation in the liver. Nature 357:605-7.
26. Ordonez A, Snapp EL, Tan L, Miranda E, Marciniak SJ, Lomas DA. 2013. Endoplasmic reticulum polymers impair luminal protein mobility and sensitize to cellular stress in alpha1-antitrypsin deficiency. Hepatology 57:2049-60.
27. Ekeowa UI, Freeke J, Miranda E, Gooptu B, Bush MF, Perez J, Teckman J, Robinson CV, Lomas DA. 2010. Defining the mechanism of polymerization in the serpinopathies. Proc Natl Acad Sci U S A 107:17146-51.

28. Suhy DA, Giddings TH, Jr., Kirkegaard K. 2000. Remodeling the endoplasmic reticulum by poliovirus infection and by individual viral proteins: an autophagy-like origin for virus-induced vesicles. J Virol 74:8953-65.
29. Windsor M, Hawes P, Monaghan P, Snapp E, Salas ML, Rodriguez JM, Wileman T. 2012. Mechanism of collapse of endoplasmic reticulum cisternae during African swine fever virus infection. Traffic 13:30-42.
30. Miller S, Krijnse-Locker J. 2008. Modification of intracellular membrane structures for virus replication. Nat Rev Microbiol 6:363-74.
31. Siddiquey MNA, Zhang H, Nguyen CC, Domma AJ, Kamil JP. 2018. The human cytomegalovirus ER resident glycoprotein UL148 activates the unfolded protein response. J Virol doi:10.1128/JVI.00896-18.
32. Cormack BP, Valdivia RH, Falkow S. 1996. FACS-optimized mutants of the green fluorescent protein (GFP). Gene 173:33-8.
33. Khaminets A, Heinrich T, Mari M, Grumati P, Huebner AK, Akutsu M, Liebmann L, Stolz A, Nietzsche S, Koch N, Mauthe M, Katona I, Qualmann B, Weis J, Reggiori F, Kurth I, Hubner CA, Dikic I. 2015. Regulation of endoplasmic reticulum turnover by selective autophagy. Nature 522:354-8.
34. Meng L, Mohan R, Kwok BH, Elofsson M, Sin N, Crews CM. 1999. Epoxomicin, a potent and selective proteasome inhibitor, exhibits in vivo antiinflammatory activity. Proc Natl Acad Sci U S A 96:10403-8.
35. Muroi M, Shiragami N, Nagao K, Yamasaki M, Takatsuki A. 1993. Folimycin (concanamycin A), a specific inhibitor of V-ATPase, blocks intracellular translocation of the glycoprotein of vesicular stomatitis virus before arrival to the Golgi apparatus. Cell Struct Funct 18:139-49.
36. Muroi M, Takasu A, Yamasaki M, Takatsuki A. 1993. Folimycin (concanamycin A), an inhibitor of V-type H(+)-ATPase, blocks cell-surface expression of virus-envelope glycoproteins. Biochem Biophys Res Commun 193:999-1005.
37. Kondratyev M, Avezov E, Shenkman M, Groisman B, Lederkremer GZ. 2007. PERK-dependent compartmentalization of ERAD and unfolded protein response machineries during ER stress. Exp Cell Res 313:3395-407.
38. Harding HP, Novoa I, Zhang Y, Zeng H, Wek R, Schapira M, Ron D. 2000. Regulated translation initiation controls stress-induced gene expression in mammalian cells. Mol Cell 6:1099-108.
39. Palam LR, Baird TD, Wek RC. 2011. Phosphorylation of eIF2 facilitates ribosomal bypass of an inhibitory upstream ORF to enhance CHOP translation. J Biol Chem 286:10939-49.
40. Vattem KM, Wek RC. 2004. Reinitiation involving upstream ORFs regulates ATF4 mRNA translation in mammalian cells. Proc Natl Acad Sci U S A 101:11269-74.
41. Sidrauski C, Acosta-Alvear D, Khoutorsky A, Vedantham P, Hearn BR, Li H, Gamache K, Gallagher CM, Ang KK, Wilson C, Okreglak V, Ashkenazi A, Hann B, Nader K, Arkin MR, Renslo AR, Sonenberg N, Walter P. 2013. Pharmacological brake-release of mRNA translation enhances cognitive memory. Elife 2:e00498.
42. Sidrauski C, McGeachy AM, Ingolia NT, Walter P. 2015. The small molecule ISRIB reverses the effects of eIF2alpha phosphorylation on translation and stress granule assembly. Elife 4.

43. Zyryanova AF, Weis F, Faille A, Alard AA, Crespillo-Casado A, Sekine Y, Harding HP, Allen F, Parts L, Fromont C, Fischer PM, Warren AJ, Ron D. 2018. Binding of ISRIB reveals a regulatory site in the nucleotide exchange factor eIF2B. Science 359:1533-1536.
44. Sidrauski C, Tsai JC, Kampmann M, Hearn BR, Vedantham P, Jaishankar P, Sokabe M, Mendez AS, Newton BW, Tang EL, Verschueren E, Johnson JR, Krogan NJ, Fraser CS, Weissman JS, Renslo AR, Walter P. 2015. Pharmacological dimerization and activation of the exchange factor eIF2B antagonizes the integrated stress response. Elife 4:e07314.
45. Tsai JC, Miller-Vedam LE, Anand AA, Jaishankar P, Nguyen HC, Renslo AR, Frost A, Walter P. 2018. Structure of the nucleotide exchange factor eIF2B reveals mechanism of memory-enhancing molecule. Science 359.
46. Gordiyenko Y, Schmidt C, Jennings MD, Matak-Vinkovic D, Pavitt GD, Robinson CV. 2014. eIF2B is a decameric guanine nucleotide exchange factor with a gamma2epsilon2 tetrameric core. Nat Commun 5:3902.
47. Harding HP, Zhang Y, Ron D. 1999. Protein translation and folding are coupled by an endoplasmic-reticulum-resident kinase. Nature 397:271-4.
48. Harding HP, Zhang Y, Bertolotti A, Zeng H, Ron D. 2000. Perk is essential for translational regulation and cell survival during the unfolded protein response. Mol Cell 5:897-904.
49. Axten JM, Medina JR, Feng Y, Shu A, Romeril SP, Grant SW, Li WH, Heerding DA, Minthorn E, Mencken T, Atkins C, Liu Q, Rabindran S, Kumar R, Hong X, Goetz A, Stanley T, Taylor JD, Sigethy SD, Tomberlin GH, Hassell AM, Kahler KM, Shewchuk LM, Gampe RT. 2012. Discovery of 7-methyl-5-(1-{[3-(trifluoromethyl)phenyl]acetyl}-2,3-dihydro-1H-indol-5-yl)-7H-p yrrolo[2,3-d]pyrimidin-4-amine (GSK2606414), a potent and selective first-in-class inhibitor of protein kinase R (PKR)-like endoplasmic reticulum kinase (PERK). J Med Chem 55:7193-207.
50. Tenorio R, Fernandez de Castro I, Knowlton JJ, Zamora PF, Lee CH, Mainou BA, Dermody TS, Risco C. 2018. Reovirus sigmaNS and muNS Proteins Remodel the Endoplasmic Reticulum to Build Replication Neo-Organelles. MBio 9.
51. Miller S, Kastner S, Krijnse-Locker J, Buhler S, Bartenschlager R. 2007. The non-structural protein 4A of dengue virus is an integral membrane protein inducing membrane alterations in a 2K-regulated manner. J Biol Chem 282:8873-82.
52. Lamond AI, Sleeman JE. 2003. Nuclear substructure and dynamics. Curr Biol 13:R825-8.
53. Granell S, Baldini G, Mohammad S, Nicolin V, Narducci P, Storrie B, Baldini G. 2008. Sequestration of mutated alpha1-antitrypsin into inclusion bodies is a cell-protective mechanism to maintain endoplasmic reticulum function. Mol Biol Cell 19:572-86.
54. Lawless MW, Greene CM, Mulgrew A, Taggart CC, O'Neill SJ, McElvaney NG. 2004. Activation of endoplasmic reticulum-specific stress responses associated with the conformational disease Z alpha 1-antitrypsin deficiency. J Immunol 172:5722-6.
55. Tirosh B, Iwakoshi NN, Lilley BN, Lee AH, Glimcher LH, Ploegh HL. 2005. Human cytomegalovirus protein US11 provokes an unfolded protein response that may facilitate the degradation of class I major histocompatibility complex products. J Virol 79:2768-79.
56. Wiertz EJ, Jones TR, Sun L, Bogyo M, Geuze HJ, Ploegh HL. 1996. The human cytomegalovirus US11 gene product dislocates MHC class I heavy chains from the endoplasmic reticulum to the cytosol. Cell 84:769-79.

57. van den Boomen DJ, Timms RT, Grice GL, Stagg HR, Skodt K, Dougan G, Nathan JA, Lehner PJ. 2014. TMEM129 is a Derlin-1 associated ERAD E3 ligase essential for virus-induced degradation of MHC-I. Proc Natl Acad Sci U S A 111:11425-30.
58. Caramelo JJ, Parodi AJ. 2008. Getting in and out from calnexin/calreticulin cycles. J Biol Chem 283:10221-5.
59. Hammond C, Braakman I, Helenius A. 1994. Role of N-linked oligosaccharide recognition, glucose trimming, and calnexin in glycoprotein folding and quality control. Proc Natl Acad Sci U S A 91:913-7.
60. Zhou M, Yu Q, Wechsler A, Ryckman BJ. 2013. Comparative analysis of gO isoforms reveals that strains of human cytomegalovirus differ in the ratio of gH/gL/gO and gH/gL/UL128-131 in the virion envelope. J Virol 87:9680-90.
61. Zhang L, Zhou M, Stanton R, Kamil J, Ryckman BJ. 2018. Expression Levels of Glycoprotein O (gO) Vary between Strains of Human Cytomegalovirus, Influencing the Assembly of gH/gL Complexes and Virion Infectivity. J Virol 92.
62. Sifers RN, Brashears-Macatee S, Kidd VJ, Muensch H, Woo SL. 1988. A frameshift mutation results in a truncated alpha 1-antitrypsin that is retained within the rough endoplasmic reticulum. J Biol Chem 263:7330-5.
63. Choudhury P, Liu Y, Bick RJ, Sifers RN. 1997. Intracellular association between UDP-glucose:glycoprotein glucosyltransferase and an incompletely folded variant of alpha1-antitrypsin. J Biol Chem 272:13446-51.
64. Tsao YS, Ivessa NE, Adesnik M, Sabatini DD, Kreibich G. 1992. Carboxy terminally truncated forms of ribophorin I are degraded in pre-Golgi compartments by a calcium-dependent process. J Cell Biol 116:57-67.
65. de Virgilio M, Weninger H, Ivessa NE. 1998. Ubiquitination is required for the retro-translocation of a short-lived luminal endoplasmic reticulum glycoprotein to the cytosol for degradation by the proteasome. J Biol Chem 273:9734-43.
66. Johnston JA, Ward CL, Kopito RR. 1998. Aggresomes: a cellular response to misfolded proteins. J Cell Biol 143:1883-98.
67. Johnston JA, Illing ME, Kopito RR. 2002. Cytoplasmic dynein/dynactin mediates the assembly of aggresomes. Cell Motil Cytoskeleton 53:26-38.
68. Pankiv S, Alemu EA, Brech A, Bruun JA, Lamark T, Overvatn A, Bjorkoy G, Johansen T. 2010. FYCO1 is a Rab7 effector that binds to LC3 and PI3P to mediate microtubule plus end-directed vesicle transport. J Cell Biol 188:253-69.
69. Hummel T, Krukkert K, Roos J, Davis G, Klambt C. 2000. Drosophila Futsch/22C10 is a MAP1B-like protein required for dendritic and axonal development. Neuron 26:357-70.
70. Wang H, Bedford FK, Brandon NJ, Moss SJ, Olsen RW. 1999. GABA(A)-receptor-associated protein links GABA(A) receptors and the cytoskeleton. Nature 397:69-72.
71. Zhang K, Daigle JG, Cunningham KM, Coyne AN, Ruan K, Grima JC, Bowen KE, Wadhwa H, Yang P, Rigo F, Taylor JP, Gitler AD, Rothstein JD, Lloyd TE. 2018. Stress Granule Assembly Disrupts Nucleocytoplasmic Transport. Cell 173:958-971 e17.
72. Li YR, King OD, Shorter J, Gitler AD. 2013. Stress granules as crucibles of ALS pathogenesis. J Cell Biol 201:361-72.
73. Hetz C, Saxena S. 2017. ER stress and the unfolded protein response in neurodegeneration. Nat Rev Neurol 13:477-491.

74. Kirchoff V, Wong S, St JS, Pari GS. 2002. Generation of a life-expanded rhesus monkey fibroblast cell line for the growth of rhesus rhadinovirus (RRV). Arch Virol 147:321-33.
75. Sinzger C, Hahn G, Digel M, Katona R, Sampaio KL, Messerle M, Hengel H, Koszinowski U, Brune W, Adler B. 2008. Cloning and sequencing of a highly productive, endotheliotropic virus strain derived from human cytomegalovirus TB40/E. J Gen Virol 89:359-68.
76. Smith IL, Taskintuna I, Rahhal FM, Powell HC, Ai E, Mueller AJ, Spector SA, Freeman WR. 1998. Clinical failure of CMV retinitis with intravitreal cidofovir is associated with antiviral resistance. Arch Ophthalmol 116:178-85.
77. Murphy E, Yu D, Grimwood J, Schmutz J, Dickson M, Jarvis MA, Hahn G, Nelson JA, Myers RM, Shenk TE. 2003. Coding potential of laboratory and clinical strains of human cytomegalovirus. Proc Natl Acad Sci U S A 100:14976-81.
78. Stanton RJ, Baluchova K, Dargan DJ, Cunningham C, Sheehy O, Seirafian S, McSharry BP, Neale ML, Davies JA, Tomasec P, Davison AJ, Wilkinson GW. 2010. Reconstruction of the complete human cytomegalovirus genome in a BAC reveals RL13 to be a potent inhibitor of replication. J Clin Invest 120:3191-208.
79. Hobom U, Brune W, Messerle M, Hahn G, Koszinowski UH. 2000. Fast screening procedures for random transposon libraries of cloned herpesvirus genomes: mutational analysis of human cytomegalovirus envelope glycoprotein genes. J Virol 74:7720-9.
80. Chang WL, Barry PA. 2003. Cloning of the full-length rhesus cytomegalovirus genome as an infectious and self-excisable bacterial artificial chromosome for analysis of viral pathogenesis. J Virol 77:5073-83.
81. Tischer BK, Smith GA, Osterrieder N. 2010. En passant mutagenesis: a two step markerless red recombination system. Methods Mol Biol 634:421-30.
82. Tischer BK, von Einem J, Kaufer B, Osterrieder N. 2006. Two-step red-mediated recombination for versatile high-efficiency markerless DNA manipulation in Escherichia coli. Biotechniques 40:191-7.
83. Dietz AN, Villinger C, Becker S, Frick M, von Einem J. 2018. A Tyrosine-Based Trafficking Motif of the Tegument Protein pUL71 Is Crucial for Human Cytomegalovirus Secondary Envelopment. J Virol 92.
84. Hohn K, Sailer M, Wang L, Lorenz M, Schneider ME, Walther P. 2011. Preparation of cryofixed cells for improved 3D ultrastructure with scanning transmission electron tomography. Histochem Cell Biol 135:1-9.
85. Villinger C, Schauflinger M, Gregorius H, Kranz C, Hohn K, Nafeey S, Walther P. 2014. Three-dimensional imaging of adherent cells using FIB/SEM and STEM. Methods Mol Biol 1117:617-38.
86. Kremer JR, Mastronarde DN, McIntosh JR. 1996. Computer visualization of three-dimensional image data using IMOD. J Struct Biol 116:71-6.
87. Britt WJ, Jarvis MA, Drummond DD, Mach M. 2005. Antigenic domain 1 is required for oligomerization of human cytomegalovirus glycoprotein B. J Virol 79:4066-79.